Paleoseismology of the Zougahana fault, northern Aso outer rim, and its role in the tectonics of northern Kyushu

Keitaro Komura[1]*, Hiroshi P. Sato[2], Hiroshi Yagi[3], Takayuki Nakano[4], Hiroshi Une[5]

[1] Central Research Institute of Electric Power Industry, 1646 Abiko, Abiko-shi 270-1194, Japan; email: komukeit@criepi.denken.or.jp

[2] Nihon University, College of Humanities and Science, 3-25-40, Sakura-Josui, Setagaya-ku, Tokyo 156-8550, Japan; email: satou.hiroshi37@nihon-u.ac.jp

[3] Fukada Geological Institute, 2-13-12, Hon-Komagome, Bunkyo-ku, Tokyo 113-0021, Japan; email: trans_himalaya@fgi.or.jp

[4] Geospatial Information Authority of Japan, 1, Kitagou, Tsukuba 305-0811, Japan; email: nakano-t96fj@mlit.go.jp

[5] Ochanomizu University, 2-1-1, Otsuka, Bunkyo-ku, Tokyo 112-8610, Japan; email: hiroune@nifty.com

* Corresponding author

Key Points

- The Zougahana fault, ~14 km northeast of the primary fault, ruptured during the 2016 Kumamoto earthquake.
- We identify ≥4 events on the Zougahana fault since 10 ka, triggered by strong motions on the primary fault.
- The Zougahana fault may not be a simple secondary fault, but part of the main transtensional shear structure.

Abstract

The Kumamoto earthquake (M_j 6.5, M_j 7.3) occurred on 14 and 16 April 2016, with the epicenter on the Futagawa and Hinagu faults, central Kyushu Island, southwest Japan. Differential interferometric synthetic aperture radar analyses detected many phase discontinuities in the source region. Phase discontinuities and ruptures were also confirmed at the Zougahana fault on the northeastern rim of Aso caldera, approximately 14 km northeast of the Futagawa fault. In this study, we conducted topographic interpretations, field surveys, outcrop descriptions/interpretations, and coring investigations of the Zougahana fault. We clarified that at least four earthquake events have occurred since 10 ka, including the 2016 earthquake. Among the events preceding the 2016 earthquake, the ages of the most recent three were estimated to be 5780–2750 cal BP, 9020–7200 cal BP, and 9430–8450 cal BP based on tephra and radiocarbon ages in the sediments. However, we note the possibility of missing events during 4350–1010 cal BP and 8690–5020 cal BP. Comparison with the paleoseismic history of the primary Futagawa fault and surrounding secondary faults suggests that the Zougahana fault is among the secondary faults that have repeatedly interacted with the Futagawa fault. The

distribution of aftershocks and our analysis of seismic intensity and Coulomb stress change indicate that the trigger for the Zougahana fault may have been strong seismic activity. However, secondary faults around Aso caldera, including the Zougahana fault, may have slipped due to various triggers. Furthermore, within the transtensional tectonics model, which views the complex of volcanoes, grabens, and strike-slip faults that fan out across central Kyushu as a single unit, the Zougahana fault may not be a simple secondary fault on the surface, but rather part of the main shear structure.

Introduction

The Futagawa and Hinagu faults are active faults in central Kyushu Island, Japan, and is located on the southern edge of the Beppu-Shimabara graben zone (BSGZ) (Matsumoto, 1979) (Fig. 1a, 1b). In 2016, successive earthquakes of M_j 6.5 (M_w 6.2) at 21:26 JST on 14 April and of M_j 7.3 (M_w 7.0) at 01:25 JST on 16 April occurred along the Futagawa and Hinagu faults (the 2016 Kumamoto earthquake sequence; Earthquake Research Committee, the Headquarters for Earthquake Research Promotion, 2016). In this contribution, we use 'the 2016 Kumamoto earthquake' or 'the 2016 earthquake' to refer to the main shock that occurred on 16 April. During this earthquake, a 30–34-km-long right-lateral rupture occurred along the Futagawa and northern part of the Hinagu faults from Mifune town in the southwest to Minami-Aso village in the northeast (Fig. 1c; Shirahama *et al*., 2016; Kumahara *et al.*, 2022). Interferometric synthetic aperture radar (InSAR) analysis of the 2016 earthquake confirmed numerous phase discontinuities around the Futagawa and Hinagu faults (Fig. 1c; Fujiwara *et al.*, 2016). Field surveys also revealed that some phase discontinuities had caused surface deformations (Goto *et al.*, 2017; Ishimura *et al.*, 2021; Une *et al.*, 2022). In this study, we refer to phase discontinuities confirmed in the field as secondary faults that are distinct from the primary fault (here the Futagawa fault) following the definition by Ishimura *et al*. (2021). Based on subsequent coring data and trench surveys, it is becoming clear that some of these secondary faults have been activated repeatedly in the past (Goto *et al*., 2017; Inoue *et al*., 2020; Ishimura *et al*., 2021; Sato *et al*., 2021).

Several interpretations have been offered for the triggering of secondary faults associated with the 2016 Kumamoto earthquake in different regions. In the area of Kumamoto city west of the Futagawa fault, the Suizenji fault zone (Fig. 1c) is thought to have slipped due to the Coulomb stress change (ΔCFF, e.g., King *et al*., 1994) associated with the rupture of the Futagawa fault (Goto *et al*., 2017). Many secondary faults with a normal fault sense appeared in the Kuradake graben northwest of Aso caldera (Fig. 1c) (Fujiwara *et al*., 2016; Une *et al*., 2022) and have been attributed to the release of background north–south tensile stress triggered by the strong seismic motions of the 2016 earthquake (Fujiwara *et al*., 2020). Furthermore, multiple NE–SW-trending phase discontinuities were identified extending from the Futagawa fault’s northeastern end to the northeastern rim of Aso caldera. The Miyaji fault (Fig. 1c), which has the same right-lateral sense as the Futagawa fault, is estimated to have repeatedly interacted with the Futagawa fault in the past (Ishimura *et al*., 2021), although the triggering mechanism is not yet understood. Toda and Ishimura (2019) showed that two secondary faulting mechanisms occurred during the 2016 Kumamoto earthquake: ΔCFF triggering and dynamic triggering, both due to the rupture of the Futagawa fault. The papers listed above suggest that secondary faulting can be triggered by diverse mechanisms, even for a single earthquake.

Clarifying the triggers of secondary faulting is important for assessing the potential for off-fault displacements and impacts on important structures (e.g., IAEA, 2010; Petersen *et al*., 2011). In particular, secondary faults occurring along the direction of extension of a strike-slip fault provide important data for evaluating the characteristics of the fault tips, such as dispersion, extension, and step (Biasi and Wesnousky, 2016, 2017; Kim and Sanderson, 2006; King and Nábělek, 1985; Lettis *et al*., 2002; Wesnousky, 1988, 2006). Together with this insight, central Kyushu Island has a unique geological structure, featuring multiple active volcanoes and grabens attributed to the oblique subduction of the Philippine Sea Plate (e.g., Hatanaka and

Shimazaki, 1988; Matsumoto, 1979; Chida, 1992; Ohashi et al., 2020). Understanding whether secondary faulting that occurred in this tectonic setting is common or unique compared to typical strike-slip fault systems will also contribute to a more accurate evaluation of off-fault displacement hazards.

In this study, we focused on a phase discontinuity that appeared about 14 km northeast of the Futagawa fault along its direction of extension, and which was previously interpreted by Fujiwara *et al*. (2016) (Fig. 2). This phase discontinuity appears to have been caused by activity on the Zougahana fault, a short fault approximately 3.5 km long (Fig. 1c; Obata, 1998) that roughly matches the trend of the phase discontinuity. The Zougahana fault occurs in a relatively fault-free area of the BSGZ (Fig. 1b) and may be an important factor in understanding the tectonics of the central Kyushu. Therefore, we conducted a paleoseismic field survey targeting the Zougahana fault to clarify its activity and association with the Futagawa fault. We also examined the trigger of the 2016 activity on the Zougahana fault from the perspectives of seismology and geology. Based on our results, we considered the role of this fault in the overall tectonics of central Kyushu.

Overview of the Zougahana D prehistoric site and geomorphology in the northeastern part of Aso caldera

The Futagawa fault, which was the source of the 2016 Kumamoto earthquake, is an active fault with an NE–SW strike that extends from Kumamoto city center to Aso caldera (Fig. 1c). In addition, several other relatively short active faults have been identified around Aso caldera (e.g., Watanabe, 1984; The Research Group for Active Tectonics in Kyushu, 1989; Suzuki *et al*., 2017). Of these, Watanabe (1984) identified a group of NE–SW-trending active faults in the northern part of Aso caldera (black solid lines in Fig. 1c). This group includes the Zougahana fault, which crosses the Zougahana D prehistoric site (containing relics from the Paleolithic era) as a NE–SW strike fault, with the northwest being the downthrown side (Obata, 1998). They stated that the displacement caused by this fault cannot be explained by gravitational slumping toward the northwest.

The Zougahana D prehistoric site is a plateau that juts southward into Aso caldera at about 800 m elevation (Fig. 1c); the plateau is situated about 300 m above the caldera floor. The lower part of the caldera wall (below 650 m elevation) is a moderate scarp, whereas the upper part of the caldera wall (650–800 m elevation) forms a steep scarp.

According to Ono and Watanabe (1985), this steep scarp is composed of ejecta from past large-scale eruptions at Aso caldera, including the lower Aso-1 pyroclastic flow deposits (ca. 280–250 ka; Matsumoto *et al*., 1991), the Aso-2/1 lava (ca. 260–190 ka and 150–140 ka; Matsumoto *et al*., 1991), the Aso-2 pyroclastic flow deposits (ca. 140 ka; Matsumoto *et al*., 1991), the Aso-3 pyroclastic flow deposits (ca. 130–120 ka; Matsumoto *et al*., 1991), and the Aso-4 pyroclastic flow deposits (approx. 87 ka; Aoki, 2008) (Fig. 3a). Most of the pyroclastic flow deposits are welded tuffs. In particular, the numerous black obsidian lithics found at the Zougahana D prehistoric site have been confirmed to originate from the Aso-2 welded tuff of this caldera wall (Watanabe *et al*., 2001). The upper part of the plateau is covered by thick volcanic ash and aeolian loam that accumulated after the Aso-4 pyroclastic flow deposits.

The volcanic ash stratigraphy in the northeastern part of Aso caldera, including the Zougahana D prehistoric site, was investigated in detail by Miyabuchi and Sugiyama (2011). They integrated the results of tephra surveys at multiple locations surrounding the Zougahana D prehistoric site and summarized the tephra stratigraphy and vegetation changes over the past 90,000 years. Figure 3b is from their schematic column, showing the shallowest 10 m below the ground surface. About twenty ash, vitric ash, scoria, and pumice layers exist, but most are petrographically similar minor tephras (e.g., YmS series; Miyabuchi, 2009) from the central cone in Aso caldera. They are therefore difficult to distinguish as chronological indicators in the stratum.

Nonetheless, three tephras described below can be used as powerful age indicators in the stratum. The most versatile is the Kikai Akahoya (K-Ah) tephra, which erupted from the Kikai caldera in southern Kyushu at around 7.3 ka and is widely distributed from the Kyushu region to western Japan; this tephra is identifying and useful for dating Holocene soils (e.g., Machida and Arai, 2003). In the Aso region in particular, it occurs as a distinct orange layer in the black soil just below the surface (e.g., Miyabuchi and Sugiyama, 2011) and is easily identified by eye (Machida and Arai, 2003). The Aira Tn (AT) tephra erupted from the Aira caldera in southern Kyushu about 30 ka; it is also a highly versatile marker tephra that is used to date glacial deposits throughout Japan (e.g., Machida and Arai, 2003). In the Aso region, it is often recognized as being slightly lighter in color than the surrounding brown soil (e.g., Miyabuchi, 2009; Miyabuchi and Sugiyama, 2011). Although more difficult to identify by eye than the K-Ah tephra, the AT tephra is easily identified based on the refractive index of bubble-wall glass and major element analysis (Machida and Arai, 2003). Another local tephra distributed around Aso is the Aso-Kusasenrigahama pumice (Kpfa; Watanabe *et al*., 1982); distal deposits are also referred to as 'Aso-K' (Machida and Arai, 2003). In the Aso area, it is recognized as a distinct orange pumice layer directly below the AT tephra (e.g., Miyabuchi, 2009; Miyabuchi and Sugiyama, 2011). Recent research on varves in Suigetsu Lake (central Japan) has constrained the eruption ages of the K-Ah and AT tephras to 7303–7165 cal BP and 30,009 ± 189 cal BP, respectively (Smith *et al*., 2013), and the eruption age of the Kpfa has been estimated as 32,647–32,376 cal BP (McLean *et al*., 2020).

Obata (1998) classified the strata at the Zougahana D prehistoric site based on the results of outcrop and pit excavations and clarified that the strata included the K-Ah, AT, and Kpfa tephras, which could be identified by eye. They also described multiple faults cutting through these tephra layers, displacing the Kpfa tephra by about 1.7 m. Because all of these faults cut the loam layer containing the K-Ah tephra, they are certainly active faults. However, Obata (1998) did not provide more detailed information related to the displacement, such as the specific displacement amount of each layer and the timing of fault activity. Maps and databases of active faults around Aso caldera published since Obata (1998) do not include the trace of the Zougahana fault (e.g., Nakata and Imaizumi, 2002; Suzuki *et al*., 2017; Imaizumi *et al*., 2018; National Institute of Advanced Industrial Science and Technology, 2025), and detailed paleoseismic investigations have not been conducted to this day.

Method

Topographic and geological survey

To understand the detailed topography around the Zougahana fault, we created a morphometric protection index red relief image map (MPI-RRIM; Kaneda and Chiba, 2019) from a 1-m-resolution airborne light detection and ranging (LiDAR) digital elevation model (DEM) acquired by the Kyushu Regional Development Bureau of the Ministry of Land, Infrastructure, Transport and Tourism in 2010, i.e., before the 2016 Kumamoto earthquake. We conducted topographic interpretation using this MPI-RRIM. Furthermore, to map the topography at the Zougahana D prehistoric site in more detail, aerial photographs were acquired after the 2016 earthquake using a DJI Phantom 4 Pro drone, from which a topographic map was generated. Before the drone photography, we set eight Real Time Kinematic-Global Navigation Satellite System reference points (Fig. 3a). Using those reference coordinates, we generated a three-dimensional image using Structure from Motion and Multi-View Stereo (SfM-MVS) photogrammetry software (Agisoft Metashape, professional version) and generated a contour map. We also cut as much grass as possible over the 2016 rupture trace before the drone photography. In addition, the wall of the surveyed outcrop and the location of the hand coring survey described below were measured using a total station (Nikon DTM-503) based on the aforementioned reference points. Furthermore, we conducted a surface survey of the area around the Zougahana D prehistoric site to track the 2016 rupture, search for fault outcrops, and confirm the surface geology.

Measurement of the 2016 rupture

Shirahama *et al*. (2016), Suzuki *et al*. (2017), and Kumahara *et al*. (2022) comprehensively mapped surface ruptures of the 2016 Kumamoto earthquake, but did not recognize surface ruptures along the Zougahana fault. However, our field survey after the 2016 earthquake revealed a rupture in the paved road within the Zougahana D prehistoric site. The rupture was not visible in the Google Earth image taken before the earthquake, suggesting that this displacement formed during the 2016 earthquake. To accurately evaluate this rupture's vertical and horizontal displacement, we measured a paved road surface using a total station, referring to the reference points shown in Figure 3a. The sideline's length was 50 m, and the distance between measurement points was 0.5 m. However, in areas with rapid displacement, more narrowly spaced points were used to measure displacement. The final measured displacement is reported as a value with a plus or minus error, was determined by the method of Kaneda *et al*. (2008) by creating best-fit lines with ±1σ uncertainty drawn from the upthrown and downthrown sides and then reading the minimum and maximum values within ±20 m of the fault and setting them as values with ± error.

Detection of the up–down component of crustal deformation using InSAR

To clarify the vertical movements around the Zougahana D prehistoric site due to the 2016 Kumamoto earthquake, a SAR interferogram was generated from PALSAR-2 data (Table 1) acquired before and after the earthquake along ascending and descending orbits, from which we estimated the quasi-vertical and horizontal movements around the Zougahana fault. We used RINC ver. 0.43 (Ozawa *et al*., 2016) to process the PALSAR-2 data and followed the 2.5-dimensional analysis method of Fujiwara *et al*. (2000) to calculate the quasi-vertical and horizontal movements. In detail, each plane includes two line-of-sight (LOS) deformation vectors perpendicular to (to the right of) the ascending and descending orbits at all ground points in the SAR image. The quasi up–down component was calculated as the two-dimensional deformation on the plane approximately vertical to the ground point.

Sketch of the Zougahana fault outcrop

Obata (1998) described the Zougahana D prehistoric site (hereafter referred to as the Zougahana fault outcrop), which is to the east of a paved road running north–south. The Zougahana fault outcrop was covered by vegetation and alluvial soil at the time of our survey. Although we planned to widen the outcrop using heavy machinery, it is in a culturally protected area by local government, and we could not do so. Therefore, we could only remove the surface vegetation and sediment from the existing outcrop and observe and describe the outcrop in order to reconstruct the 2016 rupture and prior displacements. While exposing the outcrop, we did not find any archaeological artifacts.

We exposed two walls: the north wall, about 4 m high and 7.5 m long north to south, and the south wall, about 4 m high and 3.5 m long north to south. Although the north and south walls are offset by about 1 m in the direction perpendicular to the wall's surfaces (i.e., the north wall is further back when looking at the walls toward the east), they are treated as continuous sections overlapping over a 1 m long section. Our final sketch diagram connects the two walls accordingly. Using string, we constructed a grid at 50 cm increments both walls and observed and described the detailed strata of the wall surface and the location of the 2016 rupture. In addition, we took high-resolution photographs of each grid cell to construct a 3D model and mosaic image of the wall surface using SfM-MVS (Agisoft Metashape, professional version).

Hand-coring survey

To describe the stratigraphy of the formations below the Zougahana fault outcrop and to identify key tephra layers, we used a hand auger to core down from the top of the fault outcrop to a depth of 4 m at two locations; from those cores, we collected samples for tephra analysis. We performed a similar hand auger survey at two sites along the paved road to the northwest of the fault outcrop and at two sites along the paved road to the southeast.

Radiocarbon dating and tephra analysis

To estimate the ages of the sedimentary layers, we collected charcoal materials and organic soil samples from the outcrop wall for radiocarbon dating. For tephra analysis, we collected blocks of soil measuring ca. 3 cm on each side from the hand auger cores at locations where tephra was identified by eye.

Radiocarbon ages were obtained by accelerator mass spectrometry at the Yamagata University High-Sensitivity Accelerator Mass Spectrometry Center after acid and alkali treatment and sieving through a 250 μm sieve. We obtained uncalibrated dates (yr BP).

The soil samples were sieved using a mesh cloth and an ultrasonic cleaner to extract very fine ash particles (62.5–125 μm) for tephra analysis. The extracted particles were observed under a polarizing microscope and volcanic glass shards were counted. For samples in which a significant number of volcanic glass fragments were detected, the refractive index was measured using a RIMS2000 refractometer (Kyoto Fission Track Co., Ltd., Kyoto, Japan) at the department of civil and environmental engineering, Chuo University, Tokyo, Japan. In addition, we analyzed the major element compositions of some glass samples by wavelength dispersive spectroscopy using a JEOL-JXA-8800 electron probe microanalyzer at the Central Research Institute of Electric Power Industry, Chiba, Japan. We used the same analytical conditions as Takeuchi *et al*. (2021), using the AT tephra as the standard.

Based on the ages obtained from radiocarbon dating and tephra analysis, we used OxCal v.4.4 (Bronk Ramsey, 2024) and the IntCal20 calibration curve (Reimer *et al*., 2020) to perform Bayesian estimation of the age of the event that displaced the strata. In this study, we used the Sequence Model (Bronk Ramsey, 1995) to impose constraints on the relative age of each age value when the lower strata were certainly older than the upper strata, and the Phase Model (Bronk Ramsey, 2009) to treat age values for which the relative ages were unclear (disturbed sediments or sampling locations) as a uniform group. The calendar year calibration and model age values are reported as rounded values (cal BP) with a confidence interval of ±2σ.

Results

Geomorphology, geology, and characteristics of the 2016 rupture around the Zougahana D prehistoric site

Figures 4a and 4b show the MPI-RRIM and geomorphological map around the Zougahana D prehistoric site. Around the Zougahana D prehistoric site, the plateau is being eroded from east to west. Based on the geological map (Fig. 3a), most of the plateau is covered by the Aso-4 pyroclastic flow (Fig. 4b). The erosion front can be divided into two parts: an older erosion front and a fresher erosion front that erodes the older. Part of the fresh erosion front coincides with the geological boundary between the Aso-2/1 lava and the Aso-2A/2B pyroclastic flow (Fig. 3a), which may be a geomorphological feature associated with different degrees of welding. To the northeast of the Zougahana fault outcrop is a linear scarp with a N60°E–N70°E strike and a height of 1.8–4.1 m (Figs. 4b, c, and 5a). Although it is not possible to rule out the possibility that these linear scarp features were formed by fluvial erosion, the linear valley morphology is unusual in this area, where a horseshoe-shaped erosion front dominates (Fig. 4b); therefore, the linear valley morphology is likely due to repeated fault displacement.

The mapped location of the 2016 rupture is shown in Figure 4b. A paved road adjacent to the Zougahana fault outcrop was surveyed immediately after the earthquake, and a rupture with a strike of N70°E and relatively northwest-downward displacement was observed (Fig. 5b). Many 2016 ruptures were observed directly above the Zougahana fault outcrop, and only two ruptures were found to the east of the outcrop (Fig. 4b). Nonetheless, in the gorge on the southwest side of the Zougahana fault outcrop (Loc. 1 shown in Figs. 3a, 4b), we discovered a new fault outcrop that had not been described in previous studies (Figs. 5c, d). Although this location is situated on Aso-2A/2B pyroclastic flow deposits (Fig. 3a), scarp deposits consisting mainly of secondary/reworked deposits of the more recent Aso-4 eruptive phase are exposed on the south side of the fault (Fig. 5d). On the valley floor, a small amount of welded tuff was exposed on the south side of the fault, although the lithology of this deposit was unclear. The fault at the boundary between the Aso-2A/2B pyroclastic flow deposit and the scarp deposits strikes N65°E and dips 68°S (Fig. 5d), consistent with the strike of the rupture observed on the paved road immediately adjacent to the Zougahana fault outcrop. The fault identified at Loc. 1 is a normal south-dipping fault characterized by an open rupture near the surface. The direction of vertical displacement is opposite that of the northwest-dipping rupture identified on the paved road directly below the Zougahana fault outcrop. Accordingly, the Zougahana fault is characterized by lateral movement, with the apparent direction of vertical displacement changing locally.

Figures 6a and 6b show the results of the total station survey of the 2016 rupture, which was conducted on the paved road directly below the Zougahana fault outcrop, and show the horizontal and vertical displacements. The horizontal displacement shows 48.6 ± 0.2 cm of right-lateral slip, and the vertical displacement shows the north side of the rupture dropping by 20.2 ± 4.7 cm. Therefore, the horizontal right-lateral slip is more than twice the vertical displacement, consistent with our previous interpretation that the dominant sense of slip is horizontal and that the apparent vertical displacement direction changes locally.

Figure 7 shows the pseudo-vertical deformation derived from the InSAR analysis. The northwest side of the fault subsided by up to 14 cm compared to the southeast side adjacent to the Zougahana fault, consistent with the observed vertical displacement in the field (Fig. 6b). Figure 7 includes two public triangulation points: Ogomori and Kiotoshi. According to GNSS surveying by the Geospatial Information Authority of Japan before and after the earthquake (Ootaki *et al*., 2016), the relative displacement of the Ogomori point relative to the Kiotoshi point was about 3 cm to the north and about 76 cm to the east, with 5 cm of subsidence. These survey results further support that the right-lateral horizontal displacement was much greater than the vertical displacement.

Description of the stratigraphy

The mosaic photograph and interpretive sketch of the Zougahana fault outcrop are shown in Figures 8a and 8b, respectively (see Supplement 1 for a 3D pdf file of the outcrop). The north and south walls overlap at 6.5–7.5 m horizontally across the outcrop (H6.5–H7.5), but the north wall is 1 m behind the south wall in the east–west direction (into the page). Uncalibrated radiocarbon ages (yr BP) reported in Table 2 correspond to the sample collection points in Figure 8b.

Obata (1998) conducted outcrop and small-scale pit excavation surveys around the Zougahana fault outcrop and identified 25 units cut by 15 faults. Although it was not possible to expose all the units defined by Obata (1998), we were able to observe units corresponding to layers 1–9 as described by Obata (1998). We note that the stratigraphic divisions, numbers, and fault names used herein are newly reclassified and differ from those of Obata (1998). In identifying the units, we focused on the color, consistency, powderiness, and continuity of the strata observed in the field. In our classification, we recognized 12 units: the topsoil and units 10, 20, 30, 40, 50, 60, 70, 80, 90, 200, and 210. Units 10–60 were observed in the north face, and units 80–210 in the south face, with unit 70 being common to both faces.

The surface soil includes the layer of grass and soil that covers both walls. The soil is dark brown, and the radiocarbon age of sample 1 (south wall, H8.5, V1.5) is 381 ± 20 yr BP.

Unit 10 is a black soil layer 5–15 cm thick and rich in organic matter. The radiocarbon age of sample 2 (north wall, H3.2, V1.5) is 1036 ± 20 yr BP.

Unit 20 is a dark brown soil layer 5–35 cm thick and less rich in organic matter than unit 10. The radiocarbon age of sample 3 (north wall, H3.5, V1.5) is 2220 ± 20 yr BP, and that of sample 4 (north wall, H5.7, V2.2) is 2668 ± 21 yr BP.

Unit 30 is a brown soil layer 35–80 cm thick and quite poor in organic matter. A dark orange scoria, about 3–5 mm in diameter, is scattered throughout the unit 30 soil, especially from H3.5 to H6.0.

Unit 40 is an inorganic light brown soil layer 15–25 cm thick. Orange patches 5–10 mm in diameter are scattered throughout the soil layer west of H4.0. Based on the type section for this area (Fig. 3b) and the description by Obata (1998), we correlate these patches with the K-Ah tephra.

Unit 50 is a clayey dark gray soil layer 10–35 cm thick and poor in organic matter. The boundary between units 50 and 40 is characterized by fissures and undulations such as flame structures and involution, some of which are related to deformation caused by the fault (described in the next subsection).

Unit 60 is a black soil layer 15–40 cm thick and rich in clay and organic matter. We obtained six samples from unit 60 (samples 5–10) from the north face, and their radiocarbon ages were 9297–8281 yr BP. According to Obata (1998), many artifacts from the early Jomon period have been excavated from this layer.

Unit 70 is a grayish soil layer 15–55 cm thick; it is clay-like and poor in organic matter. This unit is observed in both the north and south walls. According to Obata (1998), this layer contains microlithic relics of Paleolithic age.

Unit 80 is a brownish soil layer 40–60 cm thick and poor in organic matter. The bottom of unit 80 contains a band of scattered scoria with clasts ca. 2 mm in diameter. This scoria is stratigraphically below the K-Ah tephra and above the AT tephra (Fig. 3b); it may correlate with one of the scoria-type volcanic ashes from Aso (e.g., YmS15 at 21 ka; Miyabuchi, 2009), but a more definite correlation is difficult. Similar to the unit 50–40 boundary, undulations characterize the boundary between units 80 and 70, some of which are related to deformation by the fault (described in the next subsection).

Unit 90 is a dark brown soil layer 10–50 cm thick (though we did not observe its base) and moderately poor in organic matter. Sparse white scoria about 2 mm in diameter are included at the top of this unit.

Unit 200 is an inorganic brown soil layer 55–65 cm thick. This unit is poorly adhesive; soil particles fly out like a powder when the surface is cut with *Nisaku* twisted sickle. Some scoria 2 mm in diameter are locally distributed at the top of this unit.

Unit 210 is an inorganic gray soil layer 45–100 cm thick (though we did not observe its base) with a crunchy texture when cut with *Nisaku* twisted sickle. White pumice is scattered in this unit. Fissures and undulations characterize the boundary between units 210 and 200, similar to the unit 50–40 and 80–70 boundaries.

Based on their inorganic nature and lighter colors, units 200 and 210 imply glacial deposits. Obata (1998) reported that the units below these contain the AT and Kpfa tephras, though we could not confirm their presence by eye. Therefore, these tephras are buried even deeper than the 210 exposed unit, and all units above unit 210 must be younger than the AT tephra (approx. 30 ka).

Faults on the outcrop walls

Numerous faults and open cracks were observed in the outcrop wall. Of these, the main faults extending from the bottom of the wall surface and displacing the units were numbered F1 to F7 from north to south (Fig. 8b). Although we observed the 2016 rupture directly above the surface soil in the range of H0.0–H4.5, no clear faults were observed within the surface soil. It is possible that the displacement was dispersed by unconsolidated soil and existing vegetation, making it difficult to trace the displacement through the surface soil. We note that the fault names used herein are distinct from those of Obata (1998), and we identified the faults independently.

Fault F1 was observed in the north wall, displacing the unit 30–20 boundary by about 13 cm to the north. This displacement opened a crack up to 10 cm wide and 40 cm tall. Although we could not trace the fault upwards of unit 20, 2016 ruptures were distributed on the ground surface above the top of F1. The unit 40–30 boundary was also vertically displaced by about 4–15 cm, but it was not possible to determine whether a clear vertical displacement occurred in the units below. We also observed an open crack 3 cm wide and 10 cm tall near the unit 50–40 boundary (H2.1, V−0.1), and the patchy K-Ah tephra contained in unit 40 had fallen out of place.

Fault F2 was observed in the north wall, and an open crack 5–10 cm wide and up to 50 cm tall was observed near the unit 30–20 boundary. Slightly open cracks were also observed in units 40–60. The clearest open crack was in unit 20, but could not be traced into the units above, including unit 10. However, 2016 ruptures were distributed on the ground surface, extending from the upper end of F2. F2 deformed the top of unit 20 by about 7 cm to the north and displaced the top of unit 30 by about 12 cm to the north; it did not displace strata below unit 30.

In addition, a subordinate fault F2' split off of F2 towards the top of unit 40 and developed into an open crack 10 cm wide and 10 cm tall near the top of unit 20. Like F1 and F2, the 2016 ruptures are distributed on the ground surface extending upward from F2'. A small opening was observed in units 30–50, but became unclear near the bottom of unit 60. We measured a northward displacement of about 3.6 cm at the top of unit 30.

Fault F3 was observed in the north wall, characterized by an open crack up to 10 cm wide and 10 cm tall cutting units 10 and 20 and another open crack up to 10 cm wide and about 100 cm tall cutting units 30 and 40. Displacement was observed up to the top of unit 10, and the 2016 rupture was observed in the direction of extension. Although there was no clear vertical displacement at the unit boundaries, the top of unit 50 was displaced southward by 4.2–12.5 cm and the top of unit 60 was displaced southward by 4.2–16.7 cm. In addition, we observed a fissure-fill structure, in which units 50 and 60 open along F4 and the opening was filled by material from unit 40.

Fault F4 was observed in the north wall. We traced a slight crack in units 30–40 to at least the unit 30–20 boundary. Near the unit 60–50 boundary (H5.9, V1.2), F4 was displaced 1–2 cm to the north (i.e., to the left of the wall surface) by fault F6 (discussed below). We traced F4 to the base of the north wall, where it displaced the top of unit 60 by 9.2–36.7 cm to the north and the top of unit 70 by up to 9.2 cm to the south. We attribute this apparent reversal of the sense of displacement to the lateral offset of the units in three dimensions. Fissure-fill structures were observed in two locations in the lower units, with unit 40 filling an opening in units 50 and 60 and unit 60 filling an opening in unit 70.

Fault F5 was observed to be the longest fault in the exposed wall, extending from the base of the south wall to the unit 30–20 boundary in the north wall. An open Y-shaped crack was visible near the unit 40–30 boundary (H6.3, V1.4), and the fault showed a complex, nested form. F5 was offset to the north (to the left side of the wall) by approximately 3 cm where it crossed fault F6 (see next paragraph). Localized openings also appeared near the top of unit 80 (H6.7, V0.6), below which the fault showed complex branching in units 80 and 90. The fault displaced the top of unit 40 by about 13 cm, unit 50 by about 18 cm, unit 60 by about 18 cm, and unit 70 by about 17 cm, all in a down-to-the-north sense. Although faults F1–F4 are high-angle faults, F5 showed characteristics of a reverse fault, dipping 50–60°S. In addition, we observed a fissure-fill structure, with unit 40 dropping into units 50 and 60 and unit 60 dropping into the opening in unit 70.

Fault F6 was observed as a north-dipping fault on the north wall, and the crack extended upwards to the top of unit 20; although unclear, it seemed to continue into the surface soil and near-surface. However, we did not observe any 2016 rupture on the surface directly above F6. We also traced a clear fracture to the base of the north wall. F6 appeared to have caused a northward displacement of about 9–16 cm at the top of unit 40, displacing fault F5 by about 3 cm and fault F4 by 1–2 cm in the same direction. Therefore, F6 must postdate faults F4 and F5, indicating relatively recent slumping.

Fault F7 was observed to be a south-dipping fault separating units 70–90 from units 200–210 in the south wall. Because units 200 and 210 are interpreted to be glacial deposits, their juxtaposition next to units 70–90 imply that F7 is a reverse fault that pushed up sediments on the south side (the right side of the wall). F7 branched off gradually at H8.7 and V0.5, and the leftmost branch terminated in unit 80. The top edge of F7 showed an opening around 5–10 cm wide, and we confirmed that F7 reaches the surface soil. Unit 80, which contains the scoria band in its lower portions, was displaced vertically in multiple locations by F7, with northward displacement of about 3–17 cm at the unit 80–70 boundary and about 10–12 cm at the unit 90–80 boundary. Unit 80 was tilted about 20° northward toward the F7 fault from around H7.0, and we estimated the total vertical displacement resulting from this tilting to be over 60 cm.

Shallow subsurface structure of the fault

Figure 9a shows the locations of the six hand coring sites, and Figure 9b shows columnar sections for each core. The results of the tephra analysis conducted on each hand core are summarized in Table 3. In addition, microphotographs of particles in each tephra sample are shown in Figure S1 in Supplement materials. Major element compositions of glass shards measured by electron probe microanalysis (EPMA) are reported in Table S1 in Supplement materials.

Core ZH-1 consists of surface soil and black soil (about 0.40 m thick), dark brown soil (about 0.35 m thick), and light brown soil (at least 3.2 m thick) from top to bottom. However, as the core was excavated immediately next to a paved road, it is possible that the top layer was cut off during the excavation of the road. We observed a scoria layer approximately 3 cm thick at around 0.45 m depth, a volcanic ash layer approximately 4 cm thick and a scoria layer approximately 2 cm thick at around 1.25–1.40 m depth, a volcanic ash layer approximately 2 cm thick and a scoria layer approximately 2 cm thick at around 2.5 m depth, and a sandy volcanic ash layer approximately 10 cm thick at around 2.75 m depth. Although expected to appear in the core, we did not observe the K-Ah tephra; therefore, it is likely that the surface layer containing at least the K-Ah tephra was removed during excavation.

Core ZH-2 was cored about 10 m south of the ZH-1 core; it is likely that the surface layer was also removed during excavation at this site. From top to bottom, we identified the following layers: surface soil (about 0.10 m thick), dark brown soil (about

0.35 m thick), light brown soil (about 1.05 m thick), dark brown soil (about 0.95 m thick), and alternating layers of light brown soil and black soil (at least 1.5 m thick). Among these, we identified three scoria layers approximately 3–4 cm thick at 0.48–0.75 m depth, a scoria layer approximately 5 cm thick at 1.30 m depth, a scoria layer approximately 2 cm thick at 2.2 m depth, a sandy volcanic ash layer approximately 2 cm thick at 2.49 m depth, a sandy volcanic ash layer approximately 22 cm thick at 3.10 m depth, an orange-colored tephra layer about 14 cm thick at about 3.47 m depth, and an orange-colored tephra layer least 20 cm thick at about 3.90 m depth. We expected the sandy tephra layer at 3.10 m depth ('2-122') to be the major tephra due to its thickness of about 22 cm. The refractive index (Table 3) and major element composition of the volcanic glass (Fig. 10) are consistent with the characteristics of the AT tephra; accordingly we interpret this layer to be a pure AT tephra layer. Therefore, based on the tephra stratigraphy of the surrounding area (Fig. 3b) and the description of the AT tephra in a previous study of the Zougahana outcrop (Obata, 1998), either the orange-colored volcanic ash layer at 3.47 m depth ('2-136') or the orange-colored volcanic ash layer at 3.90 m depth ('2-150') may correspond to the Kpfa tephra. However, the major element compositions of sample 2-153 do not match the compositional range of the Kpfa tephra correlated with lake Suigetsu by McLean *et al*. (2020) and is less differentiated (lower SiO_2 content; Fig. 10). Ishimura *et al*. (2022) conducted a trench survey at the Futagawa fault west of the Aso caldera (Fig. 1c); they also recognized volcanic glass with a composition similar to that of the upper part of the Kpfa tephra, and our sample 2-153 may be correlated with the same glass as that of Ishimura *et al*. (2022). According to the model tephra stratigraphy northeast of Aso (Fig. 3b; Miyabuchi and Sugiyama, 2011), a relatively thick sandy ash is recognized directly above Kpfa, although it is not named. Samples 2-153 in this study and the upper Kpfa deposits in Ishimura *et al*. (2022) may be correlated to this sandy tephra. Regardless, because this sandy ash occurs somewhere between the AT and Kpfa tephras, it must have erupted between 32 and 30 ka.

Core ZH-3 was obtained from the top of the Zougahana fault outcrop wall and overlaps the stratigraphy identified in the wall sketch below around V1.5. From top to bottom, we recognized the following strata: surface soil (about 0.63 m thick), dark brown soil (about 1.60 m thick), black soil (about 0.47 m thick), dark brown soil (about

0.55 m thick), and light brown soil (at least 0.75 m thick). Among these, we observed a volcanic ash layer about 1 cm thick at about 0.86 m depth, a sandy volcanic ash layer about 25 cm thick at about 1.73 m depth, a sandy volcanic ash layer about 5 cm thick at about 2.27 m depth, and a scoria layer about 2 cm thick at about 3.96 m depth. The sandy tephra layer at 1.73 m depth corresponds to the K-Ah tephra in unit 40 when compared to the wall sketch (Fig. 8b). Similarly, the scoria layer at approximately 3.96 m depth in the core ('3-106') may correspond to the scoria in unit 80 of the south wall.

Core ZH-4 core was obtained from the surface of the Zougahana fault outcrop wall and overlaps the stratigraphy identified in the wall sketch below around V2.5 (Fig. 8b). From top to bottom, we identified the following layers: surface soil and black soil (about 0.60 m thick), dark brown soil (about 1.10 m thick), black soil (about 0.50 m thick), dark brown soil (about 0.45 m thick), and light brown soil (at least 0.90 m thick). Among these, we identified a volcanic ash layer about 1 cm thick at about 0.46 m depth, a sandy volcanic ash layer about 17 cm thick at about 1.35 m depth, and a scoria layer about 6 cm thick at about 3.23 m depth. The sandy volcanic ash layer 17 cm thick at 1.35 m depth in the core ('4-38') is correlated with the K-Ah tephra based on the wall sketch (Fig. 8b). Similarly, the scoria layer at 3.23 m depth in the core (‘4-94’) may correspond to the scoria in unit 80 of the south wall.

Core ZH-5 was obtained from the base of the wall at around H8.0 in the wall sketch of the Zougahana fault outcrop, and samples below unit 90 in the wall sketch. From the surface to 3.0 m depth, the soil was all light brown. Therein, we observed a volcanic ash layer approximately 1 cm thick at around 0.54 m depth, a sandy volcanic ash layer approximately 2 cm thick at around 0.75 m depth, an orange sandy volcanic ash layer approximately 2 cm thick at around 1.82 m depth, a patchy orange volcanic ash layer approximately 6 cm thick at around 1.97 m depth, a volcanic ash layer about 8 cm thick at about 2.46 m depth, and an orange volcanic ash layer about 4 cm thick at about 2.82 m depth. The refractive index of the volcanic glass in the sandy volcanic ash layer at 1.82 m depth (‘5-65’) is consistent with the AT tephra value (Table 3), and we correlate it to the AT tephra accordingly. Therefore, based on core ZH-2, the orange-colored volcanic ash at 2.80 m depth (‘5-99’), which is approximately 1 m below the AT tephra, may be comparable to the sandy ash above the Kpfa tephra.

Core ZH-6 was excavated next to a paved road on the south side of the fault. It shows the following sequence from top to bottom: surface soil (about 0.30 m thick), dark brown soil (about 0.30 m thick), light brown soil (about 2.63 m thick), and dark brown soil (at least 0.76 m thick). However, as in the ZH-1 and ZH-2 cores, some of the surface soil may have been removed during road construction. We observed a volcanic ash layer approximately 5 cm thick at around 0.47 m depth, a volcanic ash layer approximately 2 cm thick at around 0.59 m depth, a sandy volcanic ash layer approximately 2 cm thick at around 1.69 m depth, a volcanic ash layer approximately 2 cm thick at around 3.28 m depth, and a volcanic ash layer at least 5 cm thick starting at 3.89 m depth. Nonetheless, we did not identify any major tephras in core ZH-6 that could be used as age indicators, and the overall age of the core remains unknown. However, given that the F7 reverse fault exists between cores ZH-5 and ZH-6, the sediments identified in ZH-6 may be even older than the AT and Kpfa tephras.

Figure 11 presents the elevations and positions of the hand auger cores relative to the Zougahana fault outcrop sketches as a cross section based on the total station survey projected along the paved road (line A–B; Fig. 9a). In the outcrop (Fig. 8b), unit 40 and the K-Ah tephra were displaced 4–16 cm vertically by each of the F1, F5, and F6 faults (Fig. 8b) for a total displacement of 26–31 cm. Because the fault may have caused more extensive vertical deformation, these values represent the minimum displacement of the K-Ah tephra. However, the displacements of the volcanic ash and scoria layers below the K-Ah tephra were greater, emphasizing the cumulative displacement of fault. The relative heights of the scoria layers in unit 80 in the south wall and in core ZH-4 (and perhaps ZH-3) indicate a maximum vertical offset of 2.9 m across faults F1–F6 (Fig. 11). Additionally, the relative heights of the AT tephra in cores ZH-2 and ZH-5 indicate a vertical offset of approximately 2.6 m across faults F1–F6 (Fig. 11). Although the positions of the unit 80 scoria and AT tephra are unknown on the south side of fault F7, that fault is a reverse fault and the vertical displacements of both tephras are expected to be even greater than the above values when accounting for fault F7. The reason for the 30 cm displacement discrepancy between the unit 80 scoria and AT tephra remains unknown. However, given that the locations of the cores were projected along the pavement and the units are offset in 3D due to lateral movement, we consider this value to be within the margin of error. Regardless, our results clearly highlight a cumulative displacement between the deposition of the AT tephra (ca. 30 ka) and the K-Ah tephra (ca. 7.3 ka).

Paleoearthquakes and age constraints for the Zougahana fault outcrop

In our detailed observation of the Zougahana fault outcrop, we inferred multiple displacement events based on faultings and deformation structures like fissure-fill, flame, undulation, and abut observed at the top surface of each unit. In addition, the deformation structures of faults F5, F7, and the surrounding areas (Fig. 8b), which had the best continuity and were the most straightforward to interpret, were useful for recognizing events. In this subsection, we identify events, including the 2016 earthquake, from the most recent to the oldest.

The 2016 rupture at the ground surface was distributed over a width of about 4.5 m (H0.0–H4.5), but there was no clear fault corresponding to the 2016 rupture in the outcrop (Fig. 8b). Accordingly, we interpret that the displacements observable in the outcrop are part of the positive flower structure (e.g., Fossen 2016) associated with right lateral offset, and that this distributed displacement is expressed as flexural displacement at the ground surface. The wall surface also showed many fresh open cracks and fissures that had not yet been filled with sediment, which we attribute to the 2016 earthquake, consistent with a trench survey of the Futagawa fault conducted after the 2016 earthquake (Ishimura *et al*., 2022). Since all faults in the outcrop were accompanied by fresh open cracks and fissures, it is likely that all faults moved during the 2016 earthquake. In particular, faults F1–F3 on the north side have large apertures and are consistent with the locations of the 2016 ruptures at the ground surface, suggesting that most of the displacement during the 2016 earthquake occurred along these faults. Figure 12a is a sketch of the Zougahana fault outcrop (Fig. 8b) focused on the area around faults F5 and F7 in the range H5.0–H9.0, V0.0–V3.0. By removing all open cracks and fissures thought to have formed due to the 2016 earthquake, we estimate the pre-2016 earthquake wall surface appeared as in Figure 12b. Fault F6, which reached the surface and shifted fault F5 by about 3 cm and fault F4 by 1–2 cm to the north (left side of the outcrop), is thought to be a slump fault that formed as a result of the 2016 earthquake, and we have retro-deformed this displacement in Figure 12b.

We estimate that the penultimate event occurred before the deposition of unit 20 because faults F4 and F5 are interrupted at the unit 30–20 boundary, and the displacement at the unit 40–30 boundary caused by fault F5 cannot be attributed to the 2016 displacement. Hereafter, we refer to this event as ‘Event 1’. Figure 12c shows the estimated wall surface immediately after Event 1. By retro-deforming the displacement of fault F5 to zero displacement at the unit 40–30 boundary, we obtain the estimated pre-Event 1 wall surface shown in Figure 12d.

We estimate that the antepenultimate event (‘Event 2’) occurred before the deposition of unit 40. Although the unit 50–40 boundary is deformed like a flame structure, the top surface of unit 40 is inconsistently relatively flat, suggesting that deformation occurred when the unit 50–40 boundary was at the surface. Furthermore, material from unit 40 fills fissures along faults F4 and F5 in units 50 and 60. Accordingly, Figure 12e shows the estimated wall surface immediately after Event 2. By restoring the deformation at the surface of unit 50 as well as along the fissures, we estimate that the pre-Event 2 wall surface was as shown in Figure 12f. Importantly, this reconstruction requires that the K-Ah tephra was deposited after Event 2 (Fig. 12d).

According to Figure 12f, unit 50 (dark gray soil layer) is thicker to the north (left) and appears to abut unit 60. Therefore, when the deposition of unit 50 began, it is possible that the ground surface to the south (right) was already uplifting, and we estimate that the preceding event (‘Event 3’) occurred before the deposition of unit 50. We consider that the flame structure and fissures at the unit 60–50 boundary is due to Event 3, but it could have also formed underground during Event 2. Figure 12g shows the estimated wall surface immediately after Event 3. By correcting the deformation of unit 60 and rotate the section to have a flat surface, we obtain the pre-Event 3 wall surface shown in Figure 12h.

We estimated the event preceding Event 3 (‘Event 4’) based on the clear fissure-fill structure and undulation caused by fault F5 at the unit 80–70 boundary. We interpret that Event 4 occurred after the deposition of unit 80 and caused the ground surface to open; the subsequent deposition of unit 70 filled the fissure. Figure 12i shows the estimated wall surface immediately after Event 4, from which we obtained the pre-Event 4 wall surface by restoring deformation (Fig. 12j).

The F7 fault in the south wall displaced the upper surface of unit 90, and at least one of the branches of this fault appears to terminate within unit 80. Therefore, it is possible that an event occurred during the deposition of unit 80 (‘Event 5’). Figure 12k shows the estimated wall surface immediately after Event 5, from which we obtained the pre-Event 5 wall surface by restoring deformation and tilting until we achieved a flat surface for unit 80 (Fig. 12l) is estimated. Furthermore, because white scoria is scattered below unit 80, Event 5 must have occurred after deposition of this scoria.

To the south of fault F7, older deposits (units 200–210) extend further south (Fig. 8b). Furthermore, we estimated 2.6 m of cumulative vertical displacement of the AT tephra from our hand core results (Fig. 11), but this displacement cannot be explained by the cumulative vertical displacements of Events 1–5 estimated so far. Therefore, numerous events must have preceded Event 5.

Figure 13 shows the vertical displacements measured on faults F1–F7 at each stratum boundary in the wall of the Zougahana fault outcrop (Fig. 8b), as well as the unit levels of Events 1–5 and the 2016 earthquake. This figure highlights discrepancies between the displacements along fault F2 at the unit 20–10 and unit 30–20 boundaries, and along fault F5 at the unit 40–30 and unit 50–40 boundaries, for which we have not identified any event. Therefore, it is possible that 'missing' events for which we have no direct evidence in this outcrop occurred in these two sections (i.e., during the deposition of unit 20 and unit 40; 'PM Event 0.5' and 'PM Event 1.5', respectively). As we will discuss in more detail later subsection ***Comparison with paleoseismic events on the Futagawa fault and other secondary faults***, other events identified on the Futagawa fault and its surrounding secondary faults occurred during the period of deposition of unit 20 (e.g., Ishimura *et al*., 2021, 2022; Sato *et al*., 2021), supporting our interpretation of missing events on the Zougahana fault. However, such small differences in fault displacement in the trench wall can also be explained by the upper attenuation of fault displacement (Ishimura *et al*., 2017).

In summary, we identified six past events (the 2016 event and Events 1–5) in the Zougahana fault outcrop. We constructed a chronological model using OxCal based on the uncalibrated radiocarbon ages (yr BP) obtained from the wall and the results of tephra analysis to calibrate and constrain these event dates (Fig. 14a). In this model, we ignore the possible missing events ('model A'). The code for the constructed OxCal model is shown in Text S1 in Supplement materials. In this case, we adopted ages of the K-Ah tephra identified in the wall and of the AT tephra (taken as the lower limit of the earliest event) to be 7303–7165 cal BP and 30,009 ± 189 cal BP (Smith *et al.*, 2013), respectively. According to the model chronology, Event 1 (thought to have occurred at the unit 30–20 boundary) is estimated to have occurred at 5780–2750 cal BP, Event 2 (unit 50–40 boundary) at 9020–7200 cal BP, and Event 3 (unit 60–50 boundary) at 9430–8450 cal BP. Events 4 (unit 80–70 boundary), 5 (during deposition of unit 80), and the multiple earlier events for which constraining radiocarbon ages and tephra are not available are collectively estimated to have occurred between 29,850 and 10,960 cal BP (Fig. 14a) assuming the AT tephra as the oldest age constraint.

We also expanded the OxCal model to include the possible missing events during the deposition of units 20 and 40 (‘model B’, incorporating PM Events 0.5 and 1.5; Fig. 13). Although this is a hypothetical age estimation, if these two possible events did occur, the OxCal Model returned an age range of 4350–1010 cal BP for PM Event 0.5, a modified age range of 5790–2750 cal BP for Event 1, and a range of 8690–5020 cal BP for PM Event 1.5 (Fig. 14b). The OxCal code of model B is also shown in Text S2 in Supplement materials.

Discussion

Comparison with paleoseismic events on the Futagawa fault and other secondary faults

We estimated that at least six earthquake events, including the 2016 earthquake, can be concluded to have occurred on the Zougahana fault. In particular, four events are estimated to have occurred since 10 ka (model A; Fig. 14a). In addition, we expanded the model to incorporate possible missing events (PM Event 0.5, PM Event 1.5), in which case we estimated the at least eight earthquakes have occurred (model B; Fig. 14b). The average recurrence interval of events from just before the occurrence of Event 3 to just after the 2016 earthquake, which were estimated with relatively high accuracy, was calculated to be approximately 2800–3200 years for model A and approximately 1700–1900 years for model B. Assuming these average recurrence intervals to have remained constant, these values correspond to the occurrence of 9–10 events (model A) or 15–17 events (model B) since the deposition of the AT tephra ca. 30 ka. The vertical displacement of the 2016 earthquake measured on the paved road in front of the Zougahana fault outcrop was 20.2 ± 4.7 cm (Fig. 6b); if this is characteristic slip during a single event, the cumulative displacement since the AT tephra fall is 1.93 ± 0.56 m (model A) or 3.28 ± 0.95 m (model B). Given that the vertical displacement of the AT tephra based on our group-sequence coring was estimated to be about 2.6 m (Fig. 11), model B, which has an overlapping error range, appears more consistent. However, because the vertical displacement of the lateral fault may have differed in each event (e.g., Petersen *et al*., 2011), these calculations are for reference only.

Multiple trench surveys have been carried out on the Futagawa fault since the 2016 Kumamoto earthquake (Ueta *et al*., 2018; Okamura *et al*., 2018; Toda *et al*., 2019; Kumahara *et al*., 2017; Iwasa *et al*., 2022; Ishimura *et al*., 2022; Tsutsumi *et al*., 2018). Among these, Ishimura *et al*. (2022) reconstructed a reliable paleoseismic history of the Futagawa fault based on multiple pit excavation surveys. They concluded that four fault events (including the 2016 event) occurred after the K-Ah tephra fall, and estimated the ages of the three events preceding the 2016 event to be 2150–1460 cal BP, 4310–2940 cal BP, and 6030–4360 cal BP (Fig. 15a). In particular, the penultimate event (2150–1460 cal BP) has been confirmed in several other trench surveys along the Futagawa fault (Iwasa *et al*., 2022; Toda *et al*., 2019). In model A of this study, we did not identify any events corresponding to the penultimate event on the Futagawa fault, and we only found evidence for one other event since the deposition of the K-Ah tephra (Fig. 15b). Accordingly, we consider that our model B, including possible missing events (Fig. 15c), may be the better model. Of course, it is not certain that activity on the Zougahana fault has always accompanied activity of the Futagawa fault, and it may have reacted only once or several times. Nonetheless, similarly timed events were identified on the Miyaji fault (a secondary fault about 5 km south of the Zougahana fault; Fig. 1c) at 2080–1830 cal BP (Ishimura *et al*., 2021; Fig. 15d) and on the Matoishi-Bokujo I (MB I) fault (a secondary fault about 10 km away and belonging to the Kuradake graben on the northwest side of the outer rim of Aso caldera; Fig. 1c) sometime since 2810 cal BP (Sato *et al*., 2021; Fig. 15e). The paleoseismic histories of these secondary faults are consistent with our model B of the Zougahana fault, implying the existence of PM Event 0.5. Additional trench surveys to better determine the paleoseismic history of the Zougahana fault should yield further data for comparison.

What is the driving force of the Zougahana fault?

The paleoseismic record shows that the Zougahana fault has repeatedly interacted with the Futagawa fault in the past. But what drove the movement on the Zougahana fault during the 2016 Kumamoto earthquake? This pressing question needs to be answered to better evaluate the behavior of active strike-slip faults. In this section, we will consider this question from the perspectives of the aftershock distribution, strong ground motions, and ΔCFF associated with the main shock.

Background seismicity and aftershock distribution

Figure 16 shows shallow background seismicity (<20 km depth) from the northeastern part of the source region of the 2016 Kumamoto earthquake to Mt. Yufu, Oita Prefecture, as well as the distribution of aftershocks since the main shock on 16 April 2016. This figure includes the locations of the Zougahana, MB I, and Miyaji faults, which are considered to have triggered slip during the 2016 Kumamoto earthquake and may have repeatedly interacted in the past.

According to the background seismicity during the 10 years preceding the 2016 Kumamoto earthquake, earthquakes occurred only sparsely along the Futagawa fault and in the northern part of the caldera (Fig. 16a). In addition, shallow earthquakes of volcanic origin occurred around the active volcanoes Mt. Yufu and Mt. Kuju. However, there is no linear distribution of seismic sources along the strike of the Zougahana fault.

After the mainshock occurred at 01:25 JST on 16 April, active aftershocks were observed at ~10 km depth in the northern part of Aso caldera, including the Zougahana fault, without any time lag (Fig. 16b). In contrast, there exists a gap in aftershocks from the northeastern end of the Futagawa fault to the area around the Zougahana fault, known as the "Aso gap" (Uchide *et al*., 2016; Yoshida *et al*., 2017). The Aso gap has traditionally been attributed to the existence of a low-density body underground (Miyakawa *et al*., 2016); recent InSAR analyses and precise gravity observations have revealed that a hydrothermal system has created a low-stress state that prevented the propagation of the rupture (Kobayashi *et al*., 2025). In addition, a M_j 5.7 earthquake occurred near Mt. Yufu, approximately 55 km northeast of the Futagawa fault, at the same time as the main shock. It is clear in Figure 16b that aftershock activity near Mt. Yufu had begun at that time. Indeed, numerous studies have shown that the seismic motion accompanying the main shock of the 2016 Kumamoto earthquake triggered this earthquake near Mt. Yufu (Uchide *et al*., 2016; Miyazawa, 2016; Yoshida, 2016; Saito et al., 2025).

Next, 1 to 2 hours after the main shock, aftershocks continued around the Zougahana fault at ~10 km depth, with the largest (M_{j} 5.9) occurring at 03:03 JST (Fig. 16c). Furthermore, within 2–3 hours after the main shock, aftershock activity around the Zougahana fault extended further to the northeast, and at 03:55 JST, a M_{j} 5.8 aftershock occurred southwest of Mt. Kuju (Fig. 16d). Three to six hours after the main shock, aftershocks continued along the Zougahana fault and near Mt. Kuju, and at 07:11 JST, a relatively large M_{j} 5.4 aftershock again occurred near Mt Yufu (Fig. 16e). Figure 16f shows the distribution of aftershocks that occurred over the following month. Aftershocks along the Zougahana fault and near Mt. Kuju and Mt. Yufu continued. On 18 April, a M_{j} 5.8 aftershock occurred southwest of Mt. Kuju, and on 29 April, a M_{j} 4.5 aftershock occurred southeast of Mt. Yufu (Fig. 16f).

Based on the aftershock distribution, aftershock activity occurred immediately after the main shock at ~10 km depth directly below the Zougahana fault, and aftershocks propagated northeasterly from there to southwest of Mt. Kuju during the 2–

3 hours following the main shock. Mt. Kuju appears to be an obstacle (the ‘Mt. Kuju wall’) to aftershocks heading farther northeast. In addition, aftershock activity increased near Mt. Yufu, even farther from the epicenter. Given the gap in aftershock activity between Mt. Kuju and Mt. Yufu, the aftershocks from the Zougahana fault did not propagate there.

Focusing on the MB I and Miyaji faults, some shallow seismicity occurred around the MB I fault before the main shock, but no aftershocks occurred there, and almost no background earthquakes or aftershocks occurred around the Miyaji fault. Therefore, two secondary fault patterns occurred during the 2016 Kumamoto earthquake: one with aftershocks, including the Zougahana fault, and one without.

Seismic intensity

Figure 17a shows the estimated seismic intensity distribution associated with the main shock of the 2016 Kumamoto earthquake. The center of the Futagawa fault experienced strong vibrations exceeding 6+ on the Japan Meteorological Agency (JMA) seismic intensity scale, and it is estimated that the Zougahana and MB I faults were also hit by stronger tremors compared to the surrounding areas that experienced JMA seismic intensity 6−. In particular, the Zougahana fault is a hill-like landform isolated from its surroundings, and seismic motions could be further amplified by the topographic effect on earthquake motions (e.g., Boore, 1972). In contrast, the Miyaji fault, which was also triggered by the main shock, did not experience strong shaking compared to surrounding areas, registering JMA seismic intensities of 5− to 5+. In comparison, some areas in the Mt. Yufu region experienced strong seismic shaking at JMA seismic intensities of 6− to 6+, considered to result from the M_j 5.7 earthquake that occurred almost simultaneously with the main shock (Uchide *et al*., 2016; Miyazawa, 2016; Yoshida, 2016).

Δ CFF

We investigated ΔCFF to the northeast of the Futagawa fault. Many models have been proposed for the Futagawa fault rupture associated with the main shock, as well as various theories about the northeast end of the rupture (e.g., Asano and Iwata, 2016; Himematsu and Furuya, 2016; Ozawa *et al*., 2016; Yoshida *et al*., 2017; Yue *et al*., 2017; H. Kobayashi *et al*., 2017; Zhang *et al*., 2018; T. Kobayashi *et al*., 2025). Some models include the Zougahana fault and the surrounding area as the source fault, crossing Aso caldera (Kubo *et al*., 2016; Uchide *et al*., 2016). Here, however, we adopted the fault model estimated based on crustal deformation data from the Geospatial Information Authority of Japan (Yarai *et al*., 2016) and analyzed ΔCFF. The reason for this is that in the northeastern end of the model of Yarai *et al*. (2016), the western end of Aso caldera coincides well with the northeastern end of the surface rupture (Shirahama *et al*., 2016; Kumahara *et al*., 2022) (Fig. 1c). This location is also where the surface rupture dispersed, like the tip of a broom (e.g., Kim and Sanderson, 2006). We used Coulomb 3.3 software (Toda *et al*., 2011) to calculate ΔCFF, with Poisson's ratio set to 0.25 and Young's modulus to 80 GPa.

Here, we assume that the Zougahana fault is a pure right-lateral strike-slip fault. The results of the calculations showed that the Zougahana fault belongs to the -0.1 to -0.7 bar value range and shows slight negative ΔCFF values (Fig. 17b). In addition, Figures 17c and 17d show the results of our analysis when the Zougahana fault was assumed as the south- and north-dipping oblique slip fault, considering the vertical displacement from the 2016 earthquake (Fig. 5b). The shape of ΔCFF is almost the same in both cases, showing a slight negative value (-0.1 to -0.7 bar). Because the location of the fault model changes the boundary between the positive and negative regions, it is difficult to discuss the relationship between ΔCFF and the Zougahana fault based on these results. Nonetheless, the Zougahana fault is not in an area clearly characterized by positive ΔCFF; accordingly, static stress cannot have been an active trigger of the Zougahana fault. In contrast, the Miyaji fault, which has a strike nearly parallel to that of the Zougahana fault, is in a region clearly characterized by positive ΔCFF values of at least 3 bars (Figs. 17b–d). The paleoseismic history suggests that the Futagawa fault may have repeatedly triggered the Zougahana and Miyaji faults, although the triggers may have differed. Figure 17e shows the same analysis results, but when the receiver fault is set to have the sense of movement of the MB I fault. We took the strike of the MB I fault as the value measured on the map, and assumed the fault to be a pure normal fault with a 70°S dip. This assumption is based on the previous interpretation of the fault group northwest of Aso by Fujiwara *et al*. (2016). The results show that the MB I fault clearly belongs to the negative ΔCFF region (<−5.0 bar) regardless of the orientation of the receiver fault. Therefore, static stress cannot be said to be the trigger of MB I fault.

The trigger of secondary faulting at the northeast end of the Futagawa fault

The aftershock distribution, strong shaking distribution, and ΔCFF results suggest that the Zougahana fault triggered the strong shaking associated with the main shock (Fig. 17a). Nonetheless, it is interesting that a M_j 5.9 earthquake occurred around the Zougahana fault about 1.5 hours after the main shock (JST 03:03) (Fig. 16c). According to the F-net mechanism solution, this earthquake had M_w 5.5, a hypocentral depth of 5 km, a N29°E strike, and a slip plane dipping 60° to the northwest. This slip plane sense broadly corresponds to the Zougahana fault. For reference, when using the scaling law for strike-slip faults of Wells and Coppersmith (1994), a M_w 5.5 earthquake can produce a subsurface rupture length of about 2.32 km and a maximum displacement of 0.26 m. The length of the phase discontinuity that appeared along the Zougahana fault was about 4.8 km (Fig. 2), with a horizontal displacement (based on our survey) of 48.6 ± 0.2 cm and a vertical displacement of 20.2 ± 4.7 cm (Fig. 6a, b). Such displacement amounts are approximately consistent with the scaling law. In other words, it is impossible to rule out the possibility that the Zougahana fault was activated as a seismogenic with the aftershock about 1.5 hours after the main shock rather than simultaneously with the main shock. Unfortunately, there were no satellite observations between the main shock and this aftershock. Because the area around the Zougahana D prehistoric site is uninhabited, it is difficult to obtain residents’ testimonies; accordingly, it remains difficult to determine whether the Zougahana fault was activated at the time of the main shock or the aftershock.

In contrast, the trigger of the MB I fault displacement cannot be explained by ΔCFF (Fig. 17e), and there is no aftershock distribution in this area (Fig. 16b–f); it was therefore likely triggered by strong ground shaking at the same time as the main shock. Fujiwara *et al*. (2020) pointed out that the phase discontinuities to the northwest of Aso caldera, including the MB I fault, did not reflect stress changes associated with the main shock, but rather that the displacement was caused by strong ground motions, reflecting the background north–south tensile stress field; we consider their interpretation to be valid. In addition, the results for the Miyaji fault indicate that ΔCFF is a strong candidate as a trigger for displacement there (Figs. 17b–d). Therefore, although the secondary faults around Aso caldera are synchronized to activity on the Futagawa fault, their triggers are diverse. Accordingly, when evaluating secondary faults at the edge of the main fault, assessments based on only one factor will lead to underestimations of the displacement probability of that fault.

Role of the Zougahana fault in the tectonics of central Kyushu

The tectonics of the central Kyushu region, including the Futagawa fault, have been the subject of several studies that have produced various models and interpretations. Hatanaka and Shimazaki (1988) interpreted the north–south extensional movement of the BSGZ (Matsumoto, 1979) as a phenomenon in which central and northern Kyushu are displaced dextrally, parallel to the Median Tectonic Line. And they explained that the BSGZ was formed by the Philippine Sea Plate dipping obliquely to the west of the Median Tectonic Line and that the graben group, which runs in an en echelon pattern, formed to relieve the local strain of east–west compression and north–south tension. Chida (1992) divided this graben group into seven individual grabens (including the

Beppu Bay, Yufudake, Kuehirayama, Haneyama, and Kudake grabens) and proposed that these grabens formed due to the local east–west compressive stress field within the broader, north–south tensile stress field due to right-lateral movement along the Oita-Kumamoto Tectonic Line, which forms the southern limit of these grabens. Furthermore, Oohashi *et al*. (2020) discussed the tectonic history of central Kyushu by summarizing the strain field of the Futagawa fault and surrounding areas as determined by geological and geodetic methods, as well as the stress field as determined by seismological methods, in the context of existing data. They newly defined the BSGZ as the Central Kyushu Shear Zone (CKSZ), a complex of volcanoes, grabens, and strike-slip faults formed under a transtensional tectonic regime running parallel to the larger structure of the BSGZ. The 2016 Kumamoto earthquake is considered to be a tectonic movement in which dextral slip on the Futagawa-Hinagu Fault Zone (i.e., the southern boundary fault of the CKSZ), the formation of a graben, and the areal subsidence of the Kumamoto Plain to the north boundary of the CKSZ occurred simultaneously.

The CKSZ model proposed by Oohashi *et al*. (2020), which incorporates results from the 2016 Kumamoto earthquake and recent geodetic research, is the most reasonable for our interpretation. In this case, the activity of the MB I fault, which is part of the Kuradake graben, can be explained reasonably by transtensional tectonics. However, how should the Zougahana and Miyaji faults be positioned within the model? As revealed by our survey of the Zougahana fault outcrop, the Zougahana fault has repeatedly and similarly slipped since the deposition of the AT tephra ca. 30 ka. In addition, the fault outcrop at Loc. 1 (Figs. 3a, 4b) clearly shows that the fault separates the Aso-2A/2B pyroclastic flow deposit (deposited about 140 ka; Matsumoto *et al*., 1991) (Fig. 5c, d); accordingly, the Zougahana fault may have been active since the Middle Pleistocene. The Aso-4 eruption (ca. 87 ka; Aoki, 2008), which formed the present-day Aso caldera, must have destroyed and buried any active geomorphic structures around Aso caldera, including the Zougahana fault. Still, we may be witnessing a snapshot of the old scar gradually re-emerging due to motions on the Futagawa fault (or other surrounding earthquakes) or the addition of static strain. In other words, the Zougahana and Miyaji faults may not be simple secondary faults in the surface layer, but may be the main shear structures that make up the CKSZ. Figure 18 is a schematic diagram showing the locations and characteristics of the secondary faults caused by the 2016 Kumamoto earthquake superimposed on the CKSZ model of Oohashi *et al*. (2020). Although the accuracy of the locations is not sufficient, Oohashi *et al*. (2020) drew inferred dextral faults that pass through Aso caldera, and we suspect that these faults are related to the Zougahana fault and Miyaji fault. In the future, it will be necessary to clarify whether structures corresponding to these secondary faults are hidden beneath the Aso caldera and Mt. Kuju volcanic zones using seismic reflection surveys and detailed aftershock observations. In addition, future studies should consider that secondary faults can form at the contact between active faults and volcanic zones due to various factors.

Conclusions

Following the 2016 Kumamoto earthquake, phase discontinuities were confirmed by InSAR analyses of the Zougahana fault, which is approximately 14 km northeast of the primary Futagawa fault, and a surface rupture was confirmed by a field survey immediately after the 2016 earthquake. In this study, we investigated activity on the Zougahana fault by conducting topographic interpretations, field surveys, and interpretations of fault outcrops, and obtaining multiple cores. As a result, we were able to identify at least six paleoearthquake events, including the 2016 earthquake, on the Zougahana fault. The ages of the four most recent events, which were estimated with relatively high accuracy, were constrained by tephra analyses and the OxCal model using radiocarbon dating, as follows: the AD2016 earthquake and events at 5780–2750 cal BP (Event 1), 9020–7200 cal BP (Event 2), and 9430–8450 cal BP (Event 3). Furthermore, it is also thought that multiple events occurred in the period from 29,850 to 10,960 cal BP, after deposition of the AT tephra ca. 30 ka, including Events 4 and 5. Despite limited evidence, we hypothesized the occurrence of possible missing events (PM Event 0.5, PM Event 1.5) based on discrepancies among fault offsets. When compared to the paleoseismic history of the Futagawa fault and other secondary faults around Aso caldera that have slipped since the deposition of the K-Ah tephra (ca. 7.3 ka), it became clear that the number of events recognized at the Zougahana fault was likely to be an underestimate, supporting our interpretation of possible missing events at the Zougahana fault outcrop.

Based on the distribution of aftershocks, seismic intensity, and a Coulomb Stress Change (ΔCFF) analysis of the 2016 Kumamoto earthquake, we interpreted the Zougahana fault's trigger to have been strong seismic shaking associated with the main shock. However, it is currently impossible to determine whether it was triggered at the same time as the main shock or by the M_j 5.9 aftershock that occurred around the Zougahana fault about 1.5 hours later. In contrast, within the same secondary fault, the Matoishi-Bokujo I fault in the northwest of the Aso caldera may have produced normal fault displacement without an aftershock due to strong ground shaking. The Futagawa fault's ΔCFF may have triggered the Miyaji fault inside the caldera. Even if the secondary faults around Aso caldera synchronized to the activity of the Futagawa fault in the past, the specific triggers of their fault motions are diverse. When evaluating secondary faults at the ends of primary faults, assessments based on only one type of factor will likely lead to underestimates of the displacement probability of that fault.

Within the transtensional tectonics model (Central Kyushu Shear Zone), which views the larger structure of the Beppu-Shimabara Graben as a complex of volcanoes, grabens, and en echelon strike-slip faults, the Zougahana fault may not be a simple surface secondary fault. Instead, it may belong to the main shear structure. In the future, it will be necessary to carry out detailed geophysical surveys and aftershock observations to determine whether structures corresponding to surface secondary faults are buried underground in the volcanic zone.

Data and Resources

ALOS-2 data were provided by Japan Aerospace Exploration Agency (JAXA) within the framework of ERI JURP 2024-B-02 in the Earthquake Research Institute, the University of Tokyo. The 1-m-mesh LiDAR DEM used for geomorphic interpretation was obtained in 2010 by the Unzen Reconstruction Office of the Kyushu Regional Development Bureau of the Ministry of Land, Infrastructure, Transport and Tourism, and was used with the permission of the Geospatial Information Authority of Japan (GSI). The 10-m-mesh DEM used to create Figure 1 was provided by GSI. The interferogram in Figure 2 was created by GSI map (https://maps.gsi.go.jp). A visualization system for subsurface structures (https://gbank.gsj.jp/subsurface/english/ondemand.php) of AIST was used for aftershock distribution mapping (Fig. 16). The Japan Real-time Information System for earthQuake (J-RiSQ; https://www.j-risq.bosai.go.jp/report/en/R-20240323083201-0057) was used to map the seismic intensity distribution (Fig. 17a). Supplemental material for this article include a 3D Zougahana fault outcrop PDF (Supplement 1), microphotographs of particles in tephra samples (Figure S1), major element compositions of glass shards measured by EPMA (Table S1), and code for the OxCal chronological model of faulting events (Text S1, S2).

Declaration of Competing Interests

The authors declare no competing interests.

Acknowledgements

In carrying out the fault outcrop survey, we were helped by Mr. Shiraishi, the land manager of the Kiotoshi Pastural Cooperatives, and Mr. Toshikuni Miyamoto of the Aso City Board of Education; we obtained permission in advance from the Aso-Kujyu National Park Management Office of the Ministry of the Environment in accordance with the relevant laws and regulations. We want to thank Dr. Yasuo Miyabuchi, Mr. Ryuichi Teshima, Mr. Yuji Goto, Mr. Tatsuya Konoo, Mr. Hajime Fukami, Mr. Ryukei

Fukushima, Mr. Daiki Nishioka, and Mr. Miki Tokumaru from Kumamoto University for their cooperation in this fault outcrop survey. Mr. Akihiro Yamada of Ceres Corporation and Dr. Hidenobu Takahashi of the Central Research Institute of Electric Power Industry assisted with the hand auger coring survey. Ms. Yukiko Suwa of Ceres Corporation provided valuable advice on EPMA analysis.

This work was supported by JSPS KAKENHI Grant Numbers JP20K01141 and JP23K00972 (Principal Investigator: Hiroshi Une).

References

Aoki, K. (2008). Revised age and distribution of ca. 87 ka Aso-4 tephra based on new evidence from the northwest Pacific Ocean, *Quaternary International* **178**, no. 1, 100–118.

Asano, K., and T. Iwata (2016). Source rupture processes of the foreshock and mainshock in the 2016 Kumamoto earthquake sequence estimated from the kinematic waveform inversion of strong motion data, *Earth Planet Sp* **68**, no. 1, 147, doi: 10.1186/s40623-016-0519-9.

Biasi, G. P., and S. G. Wesnousky (2016). Steps and gaps in ground ruptures: Empirical bounds on rupture propagation, *Bull. Seismol. Soc. Am.* **106**, no. 3, 1110–1124.

Biasi, G. P., and S. G. Wesnousky (2017). Bends and ends of surface ruptures, *Bull. Seismol. Soc. Am.* **107**, no. 6, 2543–2560.

Boore, D. M. (1972). A Note on the Effect of Simple Topography on Seismic Sh Waves, *Bull. Seismol. Soc. Am.* **62**, no. 1, 275–284.

Bronk Ramsey, C. (2009). Bayesian Analysis of Radiocarbon Dates, *Radiocarbon* **51**, no. 01, 337–360, doi: 10.1017/S0033822200033865.

Bronk Ramsey, C. (1995). Radiocarbon Calibration and Analysis of Stratigraphy: The OxCal Program, *Radiocarbon* **37**, no. 2, 425–430, doi: 10.1017/s0033822200030903.

Bronk Ramsey, C. (2024). OxCal 4.4, available at https://c14.arch.ox.ac.uk/oxcal/OxCal.html# (last accessed April 2024).

Chida, N (1992). Active faults in Central Kyushu, Southwest Japan -Quaternary faulting along thc Median Tectonic Line in Kyushu-, *The memoirs of the Geological Society of Japan* **40**, 39–51 (in Japanese with English abstract).

Earthquake Research Committee, Headquarters for Earthquake Research Promotion (2016) Evaluation of the 2016 Kumamoto Earthquake, available at http://www.static.jishin.go.jp/resource/monthly/2016/2016_kumamoto.pdf (Last accessed 11 April 2024) (in Japanese)

Fossen, H (2016). Structural Geology, 2nd edition, Cambridge University Press, 377-400.

Fujiwara, S., T. Nakano, and Y. Morishita (2020). Detection of triggered shallow slips caused by large earthquakes using L-band SAR interferometry, *Earth, Planets and Space* **72**, no. 1, 1–23, doi: 10.1186/s40623-020-01239-6.

Fujiwara, S., T. Nishimura, M. Murakami, H. Nakagawa, M. Tobita, and P. A. Rosen (2000). 2.5-D surface deformation of M6.1 earthquake near Mt Iwate detected by SAR interferometry, *Geophysical Research Letters* **27**, no. 14, 2049–2052, doi: 10.1029/1999GL011291.

Fujiwara, S., H. Yarai, T. Kobayashi, Y. Morishita, T. Nakano, B. Miyahara, H. Nakai, Y. Miura, H. Ueshiba, Y. Kakiage, *et al.* (2016). Small-displacement linear surface ruptures of the 2016 Kumamoto earthquake sequence detected by ALOS-2 SAR interferometry, *Earth, Planets and Space* **68**, no. 1, 160, doi: 10.1186/s40623-016-0534-x.

Goto, H., H. Tsutsumi, S. Toda, and Y. Kumahara (2017). Geomorphic features of surface ruptures associated with the 2016 Kumamoto earthquake in and around the downtown of Kumamoto City, and implications on triggered slip along active faults, *Earth Planets Space* **69**, no. 1, 26, doi: 10.1186/s40623-017-0603-9.

Hatanaka, Y., and K. Shimazaki (1988). Rupture process of the 1975 central Oita, Japan, earthquake, *Journal of Physics of the Earth* **36**, no. 1, 1–15.

Himematsu, Y., and M. Furuya (2016). Fault source model for the 2016 Kumamoto earthquake sequence based on ALOS-2/PALSAR-2 pixel-offset data: evidence for dynamic slip partitioning, Earth Planets Space 68, no. 1, 169, doi: 10.1186/s40623-016-0545-7.

Imaizumi, T., T. Miyauchi, H. Tsutsumi, and T. Nakata (2018). Digital active fault map of Japan [Revised Edition], University of Tokyo Press, Tokyo.

Inoue, N., N. Kitada, N. Shibuya, M. Omata, T. Takahama, M. Tonagi, and K. Irikura (2020). Probabilistic Evaluation of Off-Fault Displacements of the 2016 Kumamoto Earthquake, *Pure Appl. Geophys.* **177**, no. 5, 2007–2019, doi: 10.1007/s00024-019-02345-7.

International Atomic Energy Agency (2010). Seismic hazards in site evaluation for nuclear installations. In IAEA Safety Standards Series No. SSG-9. ViennaResearch : IAEA.

Ishimura, D., S. Toda, T. Ichihara, N. Takahashi, A. Konno, and H. Sato (2017). A study on surface ruptures around Miyaji, Aso City, Kumamoto Prefecture, associated with the 2016 Kumamoto earthquake sequence and upward slip tapering on pit excavation walls, Act Fault Res, 47, 9–16 (in Japanese with English abstract).

Ishimura, D., H. Tsutsumi, S. Toda, Y. Fukushima, Y. Kumahara, N. Takahashi, T. Ichihara, and K. Takada (2021). Repeated triggered ruptures on a distributed secondary fault system: an example from the

2016 Kumamoto earthquake, southwest Japan, *Earth Planets Space* **73**, no. 1, 39, doi: 10.1186/s40623-021-01371-x.

Ishimura, D., Y. Iwasa, N. Takahashi, R. Tadokoro, and R. Oda (2022). Paleoseismic events and shallow subsurface structure of the central part of the Futagawa fault, which generated the 2016 Mw 7.0 Kumamoto earthquake, *Geomorphology* **414**, 108387.

Iwasa, Y., Y. Kumahara, H. Goto, D. Ishimura, and T. Hosoya (2022). Faulting history of the Futagawa fault zone based on trenching survey at Komori, Nishihara Village, Kumamoto Prefecture, *Active Fault Research* **2022**, no. 56, 47–58, doi: 10.11462/afr.2022.56_47 (in Japanese with English abstract).

Kaneda, H., and T. Chiba (2019). Stereopaired morphometric protection index red relief image maps (Stereo MPI-RRIMs): Effective visualization of high-resolution digital elevation models for interpreting and mapping small tectonic geomorphic features, *Bull. Seismol. Soc. Am.* **109**, no. 1, 99–109, doi: 10.1785/0120180166.

Kaneda, H., T. Nakata, H. Tsutsumi, H. Kondo, N. Sugito, Y. Awata, S. S. Akhtar, A. Majid, W. Khattak, A. A. Awan, R. S. Yeats, H. Ahmad, A. Muhammad, S. G. Wesnousky, A. B. Kausar (2008). Surface rupture of the 2005 Kashmir, Pakistan, earthquake and its active tectonic implications, *Bull. Seismol. Soc. Am.* **98**, no. 2, 521–557, doi: 10.1785/0120070073.

Kim, Y., and D. J. Sanderson (2006). Structural similarity and variety at the tips in a wide range of strike–slip faults: a review, *Terra Nova* **18**, no. 5, 330–344, doi: 10.1111/j.1365-3121.2006.00697.x.

King, G., and J. Nábělek (1985). Role of Fault Bends in the Initiation and Termination of Earthquake Rupture, *Science*, **228**, no. 4702, 984–987, doi: 10.1126/science.228.4702.984.

King, G. C., R. S. Stein, and J. Lin (1994). Static stress changes and the triggering of earthquakes, *Bull. Seismol. Soc. Am.* **84**, no. 3, 935–953.

Kobayashi, H., K. Koketsu, and H. Miyake (2017). Rupture processes of the 2016 Kumamoto earthquake sequence: Causes for extreme ground motions, *Geophysical Research Letters* **44**, no. 12, 6002–6010, doi: 10.1002/2017GL073857.

Kobayashi, T., K. Matsuo, R. Ando, T. Nakano, and G. Watanuki, 2025, High-resolution image on terminus of fault rupture: relationship with volcanic hydrothermal structure, Geophysical Journal International, 240, no. 2, 1196–1214.

Kubo, H., W. Suzuki, S. Aoi, and H. Sekiguchi (2016). Source rupture processes of the 2016 Kumamoto, Japan, earthquakes estimated from strong-motion waveforms, *Earth Planets Space* **68**, no. 1, 161, doi: 10.1186/s40623-016-0536-8.

Kumahara, Y., H. Kaneda, and H. Tsutsumi (Editors) (2022). *Surface Ruptures Associated with the 2016 Kumamoto Earthquake Sequence in Southwest Japan*, Springer Nature Singapore, Singapore, Advances in Geological Science, doi: 10.1007/978-981-19-1150-7.

Kumahara, Y., M. Torii, T. Nakata, H. Goto, Y. Iwasa, Y. Suzuki, M. Watanabe, S. Toda, N. Takahashi, M. Okuno (2017). Fault History of the Northern Part of Futagawa-Hinagu Fault Zone Based on Trench Survey at Dozon, Mashiki Town and at Kawayo, Minami-Aso Village, *Programme and Abstracts JSAF 2017 Fall Meeting*, Hiroshima University, Higashi-Hiroshima, 24–25 November 2017 (in Japanese).

Lettis, W., J. Bachhuber, R. Witter, C. Brankman, C. E. Randolph, A. Barka, W. D. Page, and A. Kaya (2002). Influence of releasing step-overs on surface fault rupture and fault segmentation: Examples from the 17 August 1999 Izmit earthquake on the North Anatolian fault, Turkey, *Bull. Seismol. Soc. Am.* **92**, no. 1, 19–42.

Machida, H., and Arai, F. (2003). *Atlas of Tephra in and around Japan [revised edition]*. University of Tokyo Press, Tokyo (in Japanese).

Matsumoto, A. (1979). Some Problems on Volcanic Activities and Depression Structures in Kyushu, Japan, *The memoirs of the Geological Society of Japan* **16**, 127-139 (in Japanese with English Abstruct).

Matsumoto, A., K. Uto, K. Ono, and K. Watanabe (1991). K-Ar age determinations for Aso volcanic rocks : concordance with volcanostratigraphy and application to pyroclastic flows, *Programme and Abstracts the Volcanological Society of Japan* **1991.2**, 73 (in Japanese), doi: 10.18940/vsj.1991.2.0_73.

McLean, D. et al., 2020, Constraints on the Timing of Explosive Volcanism at Aso and Aira Calderas (Japan) Between 50 and 30 ka: New Insights From the Lake Suigetsu Sedimentary Record (SG14 Core), Geochem Geophys Geosyst, 21, no. 8, e2019GC008874, doi: 10.1029/2019GC008874.

Miyabuchi, Y., 2009, A 90,000-year tephrostratigraphic framework of Aso Volcano, Japan, Sedimentary Geology, 220, nos. 3–4, 169–18.

Miyabuchi, Y., H. Hoshizumi, H. Takada, K. Watanabe, and S. Xu (2003). Pumice-fall deposits from Aso volcano during the past 90,000 years, southwestern Japan, *Kazan* **48**, no. 2, 195–214 (in Japanese with English abstract).

Miyabuchi, Y., and S. Sugiyama (2011). 90,000-year phytolith record from tephra section at the northeastern rim of Aso caldera, Japan, *Quaternary international* **246**, no. 1–2, 239–246.

Miyakawa, A., T. Sumita, Y. Okubo, R. Okuwaki, M. Otsubo, S. Uesawa, and Y. Yagi (2016). Volcanic magma reservoir imaged as a low-density body beneath Aso volcano that terminated the 2016 Kumamoto earthquake rupture, Earth Planets Space, 68, no. 1, 208, doi: 10.1186/s40623-016-0582-2.

Miyazawa, M. (2016). An investigation into the remote triggering of the Oita earthquake by the 2016 Mw 7.0 Kumamoto earthquake using full wavefield simulation, *Earth Planets Space* **68**, no. 1, 205, doi: 10.1186/s40623-016-0585-z.

Nakata, T., and T. Imaizumi (2002). Digital active fault map of Japan, University of Tokyo Press, Tokyo (in Japanese).

National Institute of Advanced Industrial Science and Technology (2009) Active Fault Database of Japan, June 23, 2009 version, available at https://gbank.gsj.jp/activefault/index_e_gmap.html (Last accessed March 2025).

National Institute of Advanced Industrial Science and Technology (2025). Active Fault Database of Japan, February 14, 2025 version, available at https://gbank.gsj.jp/activefault/index_e_gmap.html (Last accessed March 2025).

Nishiki, K., J. Itoh, and T. Ueno (2012). Database of Quaternary volcanic and intrusive rock bodies in Japan, *Geol. Surv. Jpn. Interim Rep* 60 (in Japanese).

Obata, H. (eds) (1998). The Zougahana D Prehistoric Site in Ichinomiya Town, Aso Country, Kumamoto Prefecture; Summary Report on First Excavation, Board of Education, Ichinomiya Town (in Japanese with English Abstruct).

Okamura, Y., S. Abe, Y. Miyashita, T. Azuma, T. Togo, Y. Shirahama, Y. Awata, T. Maruyama, T. Ogami, R. Imura, H. Tsutsumi, H. Goto, and Y. Kumahara (2018). Survey of detailed position and shape of active faults to understand the fault segments and observation to reveal the paleoseismic history and slip rates. In: *Research Report of a Comprehensive Active Fault Survey After the 2016 Kumamoto Earthquake*, 2017 Fiscal Year. Ministry of Education, Culture, Sports, Science and Technology and Kyushu University (in Japanese).

Ono, K. and K. Watanabe (1985). Geological Map of Aso Volcano. *Geological Map of Volcanoes* **4**. Geological Survey of Japan (in Japanese with English abstract).

Oohashi, K., M. Otsubo, S. Matsumoto, K. Kobayashi, K. Sato, and T. Nishimura (2020). The Quaternary Tectonics of Central Kyushu and the 2016 Kumamoto Earthquake: From a Multifaceted Viewpoint Combining Geology, Seismology, and Geodesy, *Journal of Geography (Chigaku Zasshi)* **129**, no. 4, 565–589, doi: 10.5026/jgeography.129.565 (in Japanese with English abstract).

Ootaki, O., T. Inoue, I. Ueda, T. Yamashita, K. Yamaguchi, H. Shirai, A. Suzuki, and K. Mikihara (2016). Revision of the Results of Control

Points after the 2016 Kumamoto Earthquake, *Journal of the Geospatial Information Authority of Japan* **128**, 177–187 (in Japanese).

Ozawa, T., E. Fujita, and H. Ueda (2016). Crustal deformation associated with the 2016 Kumamoto Earthquake and its effect on the magma system of Aso volcano, *Earth, Planets and Space* **68**, no. 1, 186, doi: 10.1186/s40623-016-0563-5.

Petersen, M. D., T. E. Dawson, R. Chen, T. Cao, C. J. Wills, D. P. Schwartz, and A. D. Frankel (2011). Fault displacement hazard for strike-slip faults, *Bull. Seismol. Soc. Am.* **101**, no. 2, 805–825.

Reimer, P. J., W. E. Austin, E. Bard, A. Bayliss, P. G. Blackwell, C. B. Ramsey, M. Butzin, H. Cheng, R. L. Edwards, and M. Friedrich (2020). The IntCal20 Northern Hemisphere radiocarbon age calibration curve (0–55 cal kBP), *Radiocarbon* **62**, no. 4, 725–757.

Saito, K., H. Takahashi, M. Ohzono, and Y. Ohta (2025). Dynamic Stress Estimation During the M 5.7 Remotely Triggered Earthquake Caused by the 2016 M 7.0 Kumamoto Earthquake, Kyushu, Japan, Using

Dense Strong-Motion and High-Rate GNSS Data, *Seismological Research Letters*, doi: 10.1785/0220240311.

Sato, H. P., K. Komura, H. Une, T. Nakano, and H. Yagi (2021). Study on Cumulative Activities of Passively Ruptured Faults through a Trenching Survey at the Matoishi Bokujo I Fault, Northwest Side of the Aso Caldera, Southwestern Japan, *Geographical review of Japan series A* **94**, no. 4, 250–264, doi: 10.4157/grj.94.250 (in Japanese with English abstract).

Shirahama, Y., M. Yoshimi, Y. Awata, T. Maruyama, T. Azuma, Y. Miyashita, H. Mori, K. Imanishi, N. Takeda, T. Ochi, *et al.* (2016). Characteristics of the surface ruptures associated with the 2016 Kumamoto earthquake sequence, central Kyushu, Japan, *Earth, Planets and Space* **68**, no. 1, doi: 10.1186/s40623-016-0559-1.

Smith, V. C., R. A. Staff, S. P. E. Blockley, C. Bronk Ramsey, T. Nakagawa, D. F. Mark, K. Takemura, and T. Danhara (2013). Identification and correlation of visible tephras in the Lake Suigetsu SG06 sedimentary archive, Japan: chronostratigraphic markers for synchronising of east Asian/west Pacific palaeoclimatic records across the last 150 ka, *Quaternary Science Reviews* **67**, 121–137, doi: 10.1016/J.QUASCIREV.2013.01.026.

Suzuki, Y., D. Ishimura, Y. Kumaki, Y. Kumahara, N. Chida, T. Nakata, and T. Nakano (2017). 1:25,000 Active Fault Map, Futagawa-Hinagu Fault Zone and its Vicinity "Aso". Geospatial Information Authority of Japan, Ibaraki (in Japanese).

Takeuchi, S., K. Toshida, D. Miura, H. Ito, and S. Uesawa, 2021, Relationships between magmatic properties and eruption magnitude of explosive eruptions at Japanese arc volcanoes during the last one hundred thousand years, Journal of Volcanology and Geothermal Research, 419, 107345.

The Research Group for Active Tectonics in Kyushu (1989). Active Tectonics in Kyushu. University of Tokyo Press, Bunkyo-ku, Tokyo (in Japanese).

Toda, S. and Ishimura, D. (2019). Evaluation of short active faults reflected from distributed minor surface breaks found at recent inland large earthquakes including the 2016 Kumamoto earthquake, *The Quaternary Research (Daiyonki-Kenkyu)* **58**, 2, 121-136 (in Japanese with English Abstract).

Toda, S., R. S. Stein, V. Sevilgen, and J. Lin (2011). Coulomb 3.3 Graphic-rich deformation and stress-change software for earthquake, tectonic, and volcano research and teaching—user guide, 63, available at https://pubs.usgs.gov/of/2011/1060/ (Last accessed April 2024).

Toda, S., M. Torii, M. Okuno, A. Konno, H. Ono, and N. Takahashi (2019). Evidence for Holocene paleoseismic events on the 2016 Kumamoto earthquake rupture zone within the Aso caldera:, *Active Fault Research* **2019**, no. 51, 13–25, doi: 10.11462/afr.2019.51_13 (in Japanese with English abstract).

Tsutsumi, H., S. Toda, H. Goto, Y. Kumahara, D. Ishimura, N. Takahashi, K. Taniguchi, M. Omata, Y. Kohriya, M. Gomi, *et al.* (2018). Paleoseismic trenching across the surface rupture of the 2016 Kumamoto earthquake at Jichu, Mashiki Town, Kumamoto Prefecture, *Active Fault Research* **2018**, no. 49, 31–39, doi: 10.11462/afr.2018.49_31 (in Japanese with English abstract).

Uchide, T., H. Horikawa, M. Nakai, R. Matsushita, N. Shigematsu, R. Ando, and K. Imanishi (2016). The 2016 Kumamoto–Oita earthquake sequence: aftershock seismicity gap and dynamic triggering in volcanic areas, *Earth Planets Space* **68**, no. 1, 180, doi: 10.1186/s40623-016-0556-4.

Ueta, K., R. Miyawaki, K. Iemura, T. Yokoyama, and A. Miyawaki (2018). Paleoseismological study on surface fault ruptures produced by the 2016 Kumamoto earthquake. In *Japan Geoscience Union Meeting 2018*, Makuhari Messe, Chiba, 20–24 May 2018 (in Japanese with English abstract).

Une, H., T. Nakano, S. Fujiwara, H. P. Sato, and H. Yagi (2022). Surface Ruptures in the Northwest of the Outer Aso Caldera, in *Surface*

Ruptures Associated with the 2016 Kumamoto Earthquake Sequence in Southwest Japan Y. Kumahara, H. Kaneda, and H. Tsutsumi(Editors), Springer Nature Singapore, Singapore, Advances in Geological Science, 205–211, doi: 10.1007/978-981-19-1150-7_15.

Watanabe, K., K. Ono, and S. Hiratsuka. (1982). Pumice eruption at Kusasenrigahama volcano, Bulletin of the Volcanological Society of Japan, 27, 337–339 (in Japanese).

Watanabe K. (1984). Active Faults in and around Kumamoto, *Journal of the Kumamoto Geoscience Association* **76**, 9–16 (in Japanese) (Translated by KK).

Watanabe, K., K. Taguchi, H. Obata, S. Okamoto (2001). Examination of obsidian and its gemstones excavated from the Zougahana D prehistoric site, Aso, Japan (Preliminary report), *Journal of the Kumamoto Geoscience Association* **127**, 2–9 (in Japanese) (Translated by KK).

Wells, D. L., and K. J. Coppersmith, 1994, New empirical relationships among magnitude, rupture length, rupture width, rupture area, and surface displacement, *Bull. Seismol. Soc. Am.* 84, no. 4, 974–1002.

Wesnousky, S. G. (1988). Seismological and structural evolution of strike-slip faults, *Nature*, **335**, no. 6188, 340–343, doi: 10.1038/335340a0.

Wesnousky, S. G. (2006). Predicting the endpoints of earthquake ruptures, *Nature*, **444**, no. 7117, 358–360.

Yarai, H. (2016). Source fault models of the 2016 Kumamoto earthquake inverted from crustal deformation, *Bulletin of the Geospatial Information Authority of Japan* **128**, 169 (in Japanese).

Yoshida, S. (2016). Earthquakes in Oita triggered by the 2016 M7.3 Kumamoto earthquake, *Earth Planets Space* **68**, no. 1, 176, doi: 10.1186/s40623-016-0552-8.

Yoshida, K., K. Miyakoshi, K. Somei, and K. Irikura (2017). Source process of the 2016 Kumamoto earthquake (Mj7.3) inferred from kinematic inversion of strong-motion records, *Earth Planets Space* **69**, no. 1, 64, doi: 10.1186/s40623-017-0649-8.

Yue, H., Z. E. Ross, C. Liang, S. Michel, H. Fattahi, E. Fielding, A. Moore, Z. Liu, and B. Jia (2017). The 2016 Kumamoto $M_w = 7.0$ Earthquake: A Significant Event in a Fault–Volcano System, *JGR Solid Earth* **122**, no. 11, 9166–9183, doi: 10.1002/2017JB014525.

Zhang, Y., X. Shan, G. Zhang, W. Gong, X. Liu, H. Yin, D. Zhao, S. Wen, and C. Qu (2018). Source model of the 2016 Kumamoto, Japan, earthquake constrained by InSAR, GPS, and strong-motion data: Fault slip under extensional stress, *Bull. Seismol. Soc. Am.* **108**, no. 5A, 2675–2686.

List of Figure Captions

Figure 1 **(a)** Location of the study area in Kyushu, southwestern Japan. EU, Eurasia plate; PA, Pacific plate; PH, Philippine Sea plate. **(b)** Topography and location of the study area in Kyushu. BSGZ, Beppu-Shimabara Graben Zone; MTL, Median Tectonic Line. **(c)** Location and topographic map of the epicentral area of the 2016 Kumamoto earthquake. Black lines indicate traces of active and inferred active faults from Nakata and Imaizumi (2002), red lines indicate surface rupture traces of the 2016 Kumamoto earthquake from Kumahara *et al.* (2022), and blue lines represent phase discontinuities identified by Fujiwara *et al.* (2016). The trace of the Zougahana fault, the main target of this study, is based on Watanabe (1984). MB I, Matoishi-Bokujo I fault. The background slope map was created from the Geospatial Information Authority of Japan (GSI) 10-m-mesh digital elevation model (DEM).

Alt-text: A series of maps showing the location and topography of the study area in Kyushu, Japan, including tectonic plates, fault traces, and the epicentral region of the 2016 Kumamoto earthquake, with annotations for key fault names and sources.

Figure 2 Interferogram of the Zougahana fault area before and after the 2016 earthquake (location shown in Fig. 1c). The images were taken on 7 March and 18 April 2016 looking south, and created based on GSI maps.

Alt-text: Interferogram images showing ground deformation around the Zougahana fault before and after the 2016 Kumamoto earthquake, with fringe patterns indicating displacement aligned along fault traces.

Figure 3 **(a)** Geological map around the Zougahana D prehistoric site based on Ono and Watanabe (1985) and Obata (1998) (location shown in Fig. 1c). The traces of phase discontinuities and the Zougahana fault are after Fujiwara *et al.* (2016) and Obata (1998), respectively. **(b)** The model tephra stratigraphy of the northeastern part of Aso caldera, based on Miyabuchi and Sugiyama (2011).

Alt-text: A geological map around the Zougahana D prehistoric site showing fault and phase discontinuity traces, and a tephra stratigraphy diagram of northeastern Aso caldera with labeled volcanic ash layers.

Figure 4 **(a)** MPI-RRIM around the Zougahana D prehistoric site based on a 1-m-mesh LiDAR DEM (location shown in Fig. 3a). **(b)** Detailed geomorphic map of the same area. Background contours at 1 m intervals were created from the same LiDAR DEM. **(c)** Topographic cross sections of the scarp along the Zougahana fault (see **(b)** for lines of section).

Alt-text: High-resolution geomorphic data around the Zougahana D prehistoric site including LiDAR-based MPI-RRIM, detailed fault mapping, and topographic cross sections highlighting the scarp of the Zougahana fault.

Figure 5 **(a)** Drone image of the Zougahana fault outcrop viewed from the west. Intermittent cracks created by the 2016 earthquake apparent in this view are indicated by red arrows. **(b)** Photograph of the 2016 rupture that appeared on the paved road in front of the Zougahana fault outcrop. **(c)** Fault outcrop found about 290 m southwest of the Zougahana fault outcrop (Loc. 1 shown in Figs. 3a, 4b). **(d)** Geologic interpretation of the outcrop in **(c)**.

Alt-text: Drone and ground photographs of the Zougahana fault outcrop and 2016 surface ruptures, with red arrows marking visible cracks and a geological sketch interpreting fault exposure at a nearby location.

Figure 6 **(a)** Results of horizontal deformation measurements based on the total station survey along the paved road. The background image is an aerial photo taken by drone in April 2021 (location shown in Fig. 4b). **(b)** Measured vertical deformation along the transect shown in **(a)**.

Alt-text: Results of total station-based horizontal and vertical deformation measurements along a paved road near the Zougahana fault, overlaid on aerial imagery taken by drone in 2021.

Figure 7 Pseudo-vertical deformation calculated from the InSAR image of the same area shown in Figure 3a.

Alt-text: Map of pseudo-vertical displacement in the Zougahana area calculated from InSAR data, showing patterns of uplift and subsidence corresponding to surface deformation features.

Figure 8 **(a)** Photomosaic and **(b)** sketch interpretation of the Zougahana fault outcrop. In **(a)** and **(b)**, numbers indicated by the open squares correspond to the radiocarbon sample numbers in Table 2. Ages in **(b)** are mean values of the radiocarbon ages (yr BP).

Alt-text: Photomosaic and corresponding geological sketch of the Zougahana fault outcrop, with labeled sample locations and radiocarbon ages used in paleoseismic analysis.

Figure 9 **(a)** Hand coring locations (blue circles). The extent of this map is the same as in Figure 6a. The background image is an altitude step-color map created based on drone aerial photography images. **(b)** Geological columns of the hand auger cores. Sample numbers (in red text) and correlated tephras are also shown.

Alt-text: Map of hand coring locations near the Zougahana fault and corresponding geological columns, showing tephra layers and sample names used in sediment and tephra correlation.

Figure 10 Major element compositions of glass shards from core ZH-2 determined by EPMA analysis.

Alt-text: Scatter plots of major element compositions of volcanic glass shards from core ZH-2 based on EPMA analysis, illustrating geochemical variation among tephra layers.

Figure 11 Inferred subsurface structure along line A–B (see Fig. 9a) based on hand cores and the interpretive sketch of the outcrop. The black circles indicate the survey points based on total station surveying and the locations of the hand cores.

Alt-text: Cross-sectional diagram of the inferred subsurface structure along a survey line, showing hand core locations and interpreted stratigraphy based on trench and core data.

Figure 12 Retro-deformation sequence of faulting and sedimentation around faults F4 to F7 in the interpretive sketch of the wall (see Fig. 8b). See subsection ***Paleoearthquakes and age constraints about Zougahana fault outcrop*** in the **Results**.

Alt-text: Schematic sequence of faulting and sedimentation events affecting faults F4–F7, illustrating paleoearthquake chronology and sediment accumulation in the wall exposure.

Figure 13 Plot of vertical offsets for each fault in each unit.

Alt-text: Graph showing vertical displacement measurements for each fault in different stratigraphic units, indicating relative fault activity through time.

Figure 14 **(a)** Age model A of the Zougahana fault outcrop constructed with OxCal software based on ^{14}C ages, tephras, and constrained ages for each event. 'R_date' indicates the ^{14}C age of each sample number (Fig. 8b and Table 2), and 'U' indicates tephra ages. Event ages are rounded to the nearest decade and presented with a 2σ (95.4%) confidence interval. **(b)** Age model B includes possible missing events. Here, we have extracted and shown only events since Event 2.

Alt-text: Two age models (A and B) of the Zougahana fault outcrop based on radiocarbon and tephra data, showing estimated event ages with uncertainties and possible missing events.

Figure 15 Comparison of the paleoseismic histories of **(a)** the primary fault (Futagawa fault; Ishimura *et al.*, 2022) and its secondary faults: **(b, c)** models A and B, respectively, for the Zougahana fault (this study), **(d)** Miyaji fault (Ishimura *et al.*, 2021), and **(e)** Matoishi-Bokujo I fault (Sato *et al.*, 2021).

Alt-text: Comparative diagram of paleoseismic event timing for the Futagawa fault and multiple secondary faults, including the Zougahana and Matoishi-Bokujo I faults, with models A and B presented.

Figure 16 (a) Background seismicity from Aso caldera to Mt. Yufu in the 10 years preceding the Kumamoto earthquake. **(b–f)** The distribution of aftershocks in the same area: **(b)** up to 1 hour after the main shock, **(c)** 1–2 hours after the main shock, **(d)** 2–3 hours after the main shock, **(e)** 3–6 hours after the main shock, and **(f)** 6 hours to 1 month after the main shock. Cross sections to 20 km depth orthogonal to the Zougahana fault are shown for all figures. The targeted earthquakes are those shallower than 20 km depth and stronger than M_j 2. These figures were drawn using the Visualization System for Subsurface Structures of the National Institute of Advanced Industrial Science and Technology (AIST). Black lines in the figure are active fault traces from the National Institute of Advanced Industrial Science and Technology (2009) and red triangles indicate the locations of Quaternary volcanoes, from Nishiki *et al.* (2012).

Alt-text: Maps and cross sections of seismicity from Aso caldera to Mt. Yufu before and after the 2016 Kumamoto earthquake, showing aftershock distributions over time and depth slices perpendicular to the Zougahana fault.

Figure 17 (a) Estimated seismic intensity distribution of the main shock of the 2016 Kumamoto earthquake by the National Research Institute for Earth Science and Disaster Prevention, based on the J-RISQ (Japan Real-time Information System for earthQuake) homepage. **(b–e)** Coulomb stress change (ΔCFF) in the northeastern part of the epicentral area associated with the slip of the Futagawa fault. The fault model was adopted from Yarai *et al.* (2016). **(b–d)** ΔCFF resolved **(b)** onto a pure dextral strike-slip fault, **(c)** onto a dextral and oblique-slip with south-dipping fault, and **(d)** onto a dextral and oblique-slip with north-dipping fault. In **(b–d)**, the strike of the receiver fault set is the Zogahana fault. **(e)** ΔCFF resolved onto a normal fault with the same strike and dip as the MB I fault.

Alt-text: Maps of estimated seismic intensity and Coulomb stress changes (ΔCFF) for the 2016 Kumamoto earthquake, showing effects on the Zougahana and MB I faults using different receiver fault assumptions.

Figure 18 Schematic illustration showing the characteristics of secondary faults and illustrating the relationship between the tectonics of central Kyushu and the tectonics from Aso caldera to Mt. Yufu. The Central Kyushu Shear Zone and the dextral fault (inferred) are drawn from Oohashi *et al.* (2020). Black thin lines indicate active faults, and red triangles indicate the locations of Quaternary volcanoes, whose sources are the same as in Figure 16.

Alt-text: Schematic diagram illustrating tectonic relationships between the Central Kyushu Shear Zone, secondary faults, and Quaternary volcanoes from Aso to Mt. Yufu, based on regional fault and volcanic data.

Figure 1

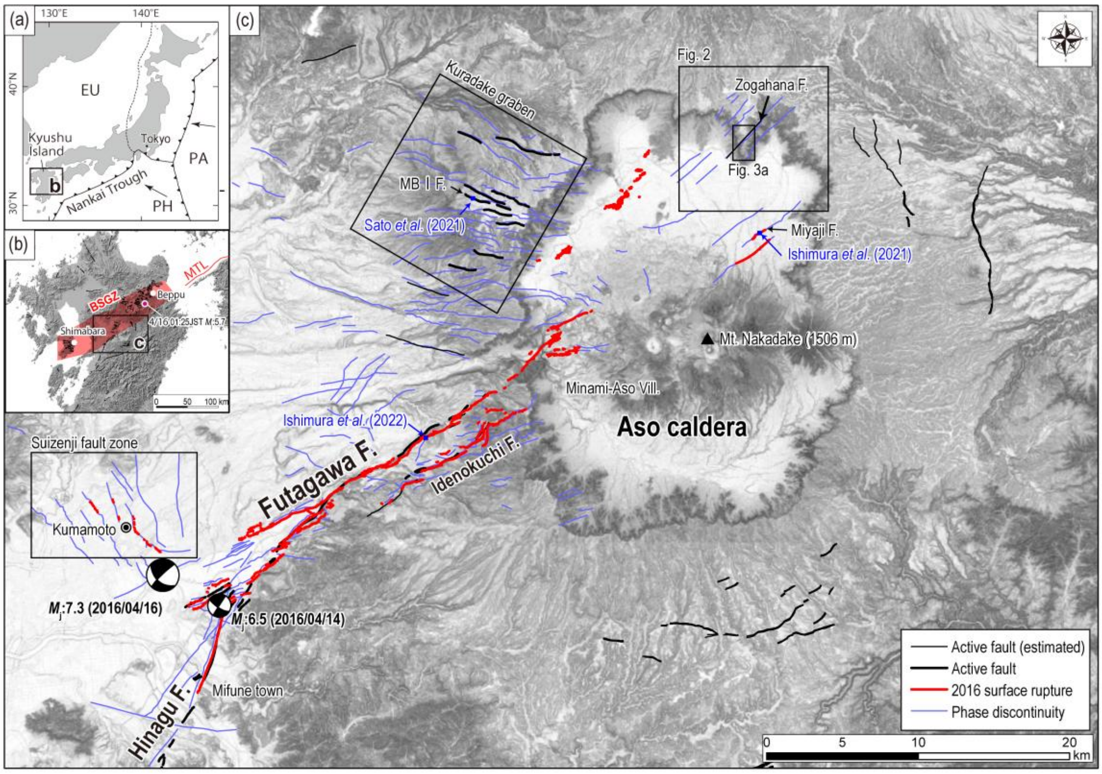

(a)
130°E
140°E
40°N
30°N
EU
Kyushu Island
b
Tokyo
PA
Nankai Trough
PH
(b)
MTL
BSGZ
Beppu
4/16 01:25JST M:5.7
Shimabara
c
0 50 100 km
(c)
Kuradake graben
MB I F.
Sato et al. (2021)
Fig. 2
Zogahana F.
Fig. 3a
Miyaji F.
Ishimura et al. (2021)
Mt. Nakadake (1506 m)
Minami-Aso Vill.
Aso caldera
Ishimura et al. (2022)
Futagawa F.
Idenokuchi F.
Suizenji fault zone
Kumamoto
M_j:7.3 (2016/04/16)
M_j:6.5 (2016/04/14)
Mifune town
Hinagu F.
Active fault (estimated)
Active fault
2016 surface rupture
Phase discontinuity
0 5 10 20 km

Figure 2

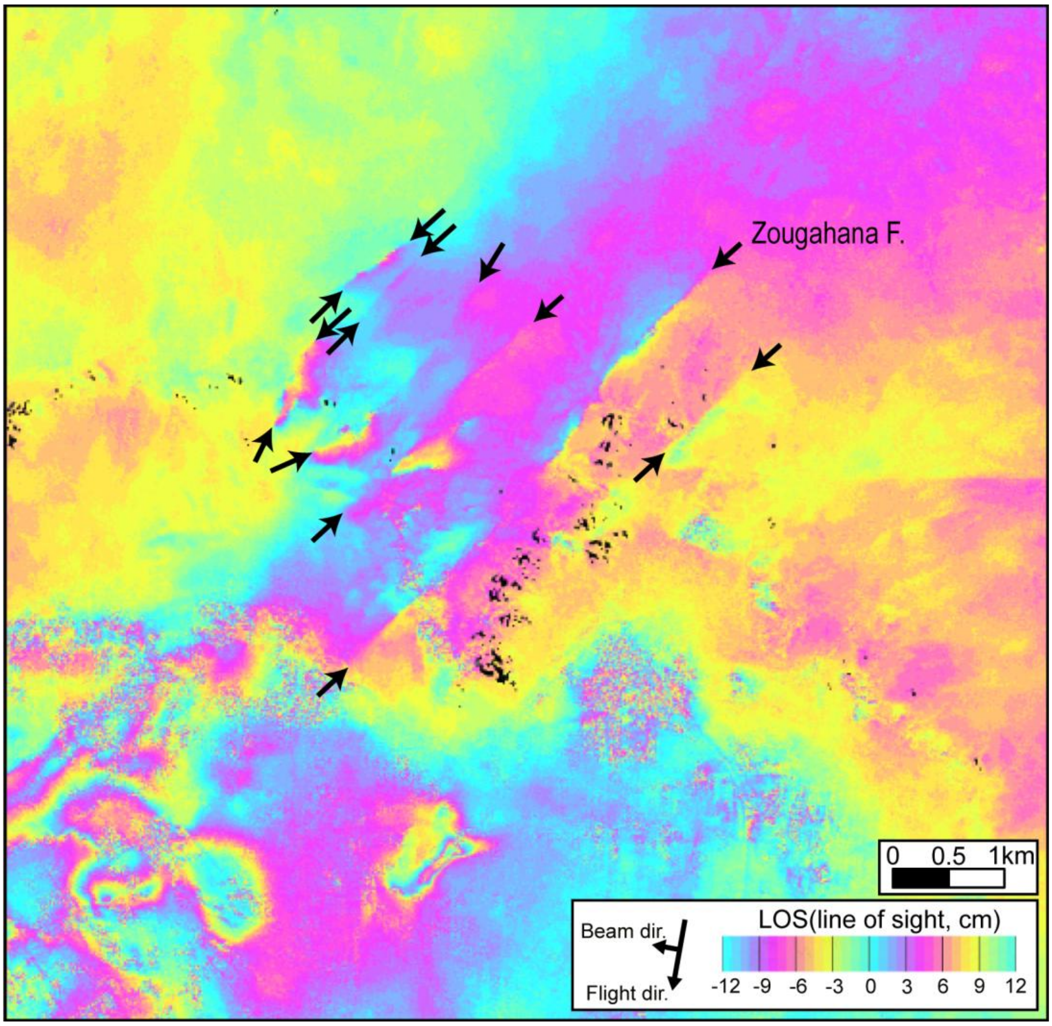
Zougahana F.
0 0.5 1km
Beam dir.
Flight dir.
LOS(line of sight, cm)
-12 -9 -6 -3 0 3 6 9 12

Figure 3

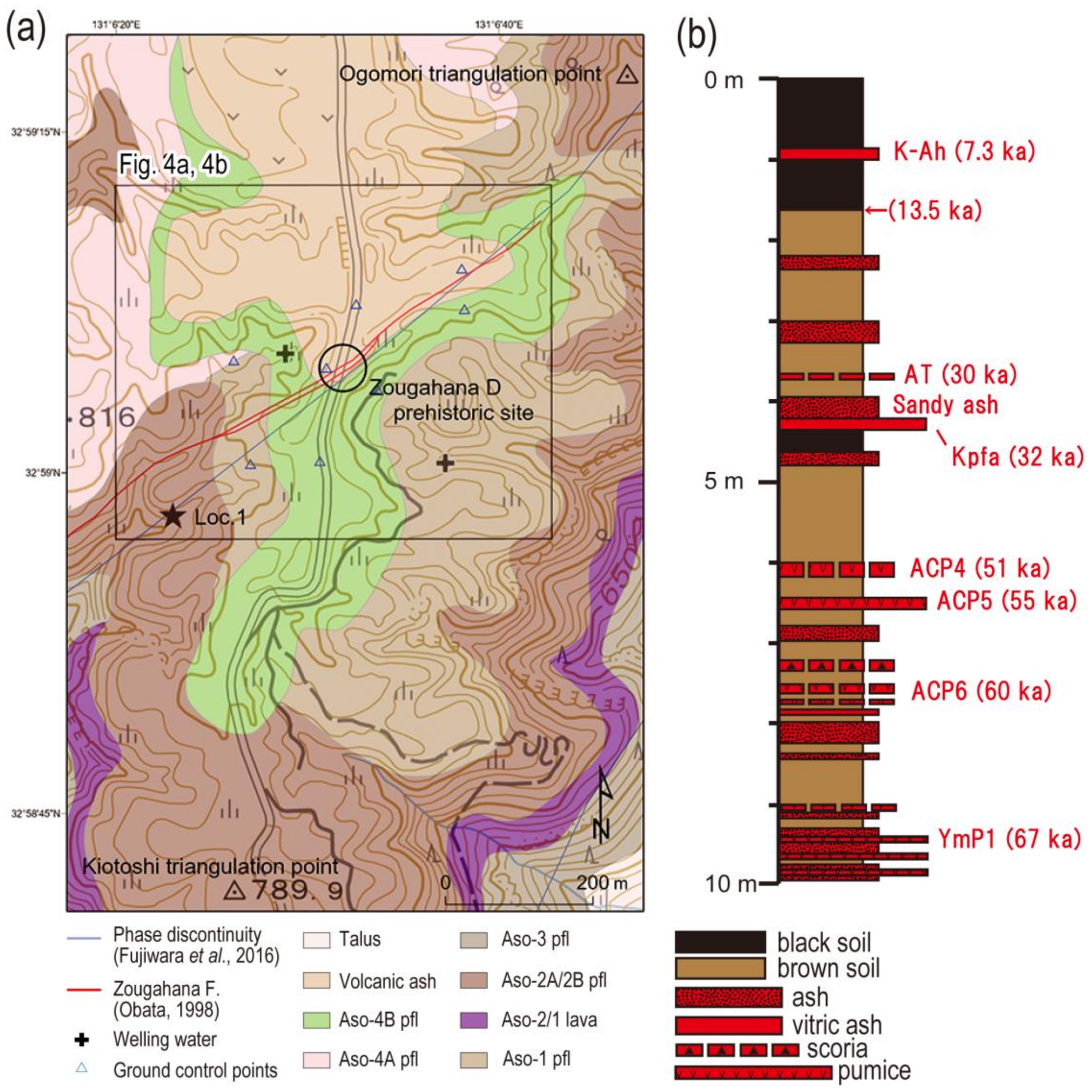

(a)
131°6'20"E
131°6'40"E
32°59'15"N
32°59'N
32°58'45"N
Ogomori triangulation point
Fig. 4a, 4b
Zougahana D prehistoric site
816
Loc.1
Kiotoshi triangulation point
789.9
0
200 m
N
Phase discontinuity (Fujiwara et al., 2016)
Zougahana F. (Obata, 1998)
Welling water
Ground control points
Talus
Volcanic ash
Aso-4B pfl
Aso-4A pfl
Aso-3 pfl
Aso-2A/2B pfl
Aso-2/1 lava
Aso-1 pfl
(b)
0 m
5 m
10 m
K-Ah (7.3 ka)
(13.5 ka)
AT (30 ka)
Sandy ash
Kpfa (32 ka)
ACP4 (51 ka)
ACP5 (55 ka)
ACP6 (60 ka)
YmP1 (67 ka)
black soil
brown soil
ash
vitric ash
scoria
pumice

Figure 4

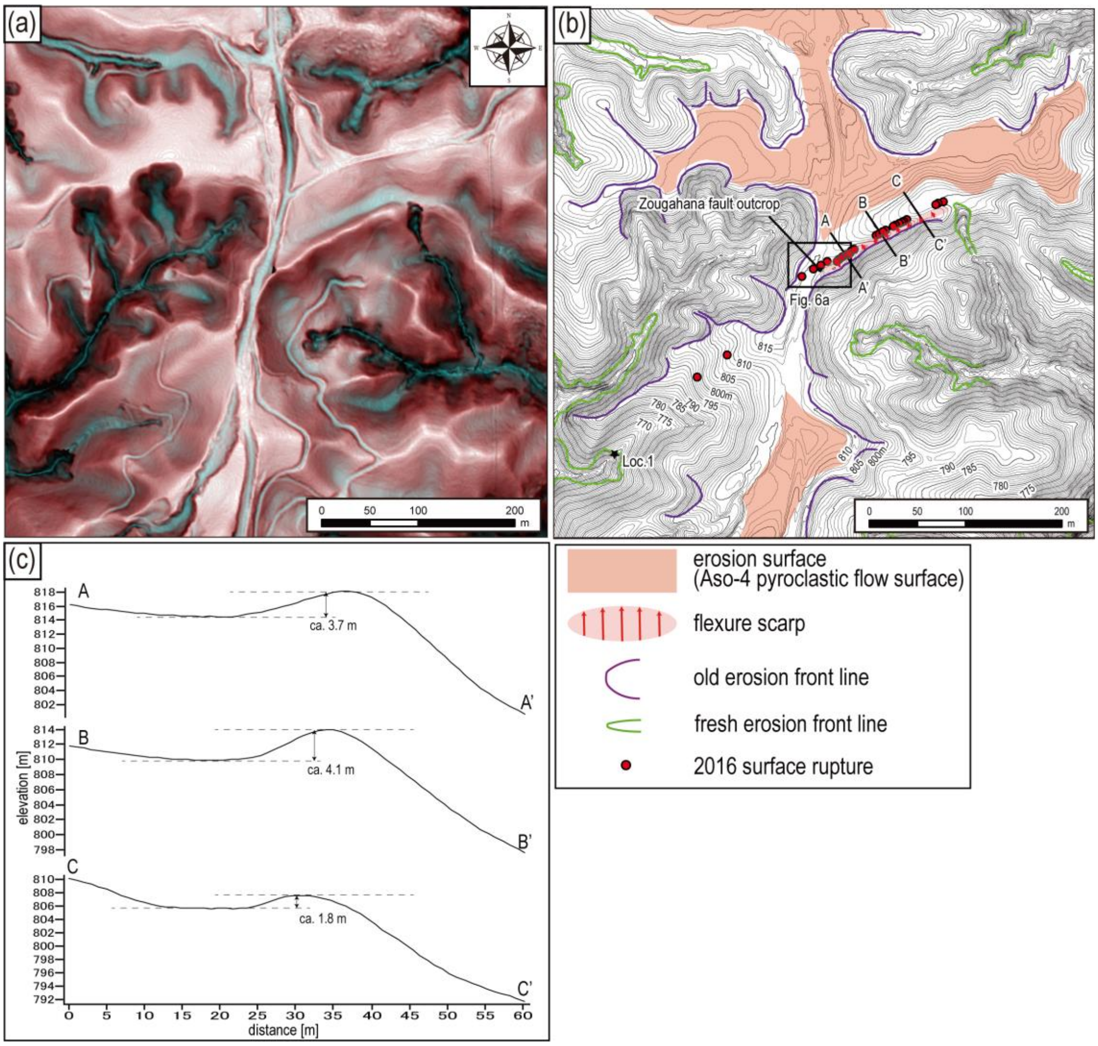
(a)
(b)
Zougahana fault outcrop
Fig. 6a
A
A'
B
B'
C
C'
Loc.1
0 50 100 200 m
(c)
elevation [m]
distance [m]
ca. 3.7 m
ca. 4.1 m
ca. 1.8 m
erosion surface
(Aso-4 pyroclastic flow surface)
flexure scarp
old erosion front line
fresh erosion front line
2016 surface rupture

Figure 5

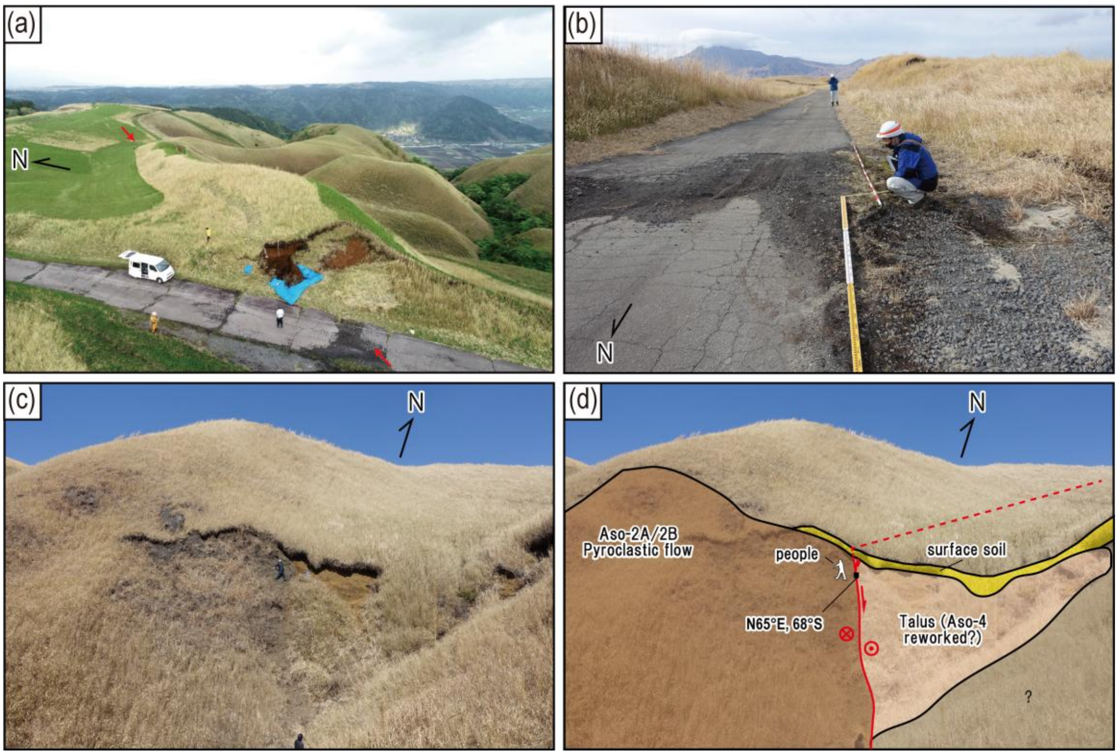
(a)
N
(b)
N
(c)
N
(d)
N
Aso-2A/2B
Pyroclastic flow
people
surface soil
N65°E, 68°S
Talus (Aso-4
reworked?)
?

Figure 6

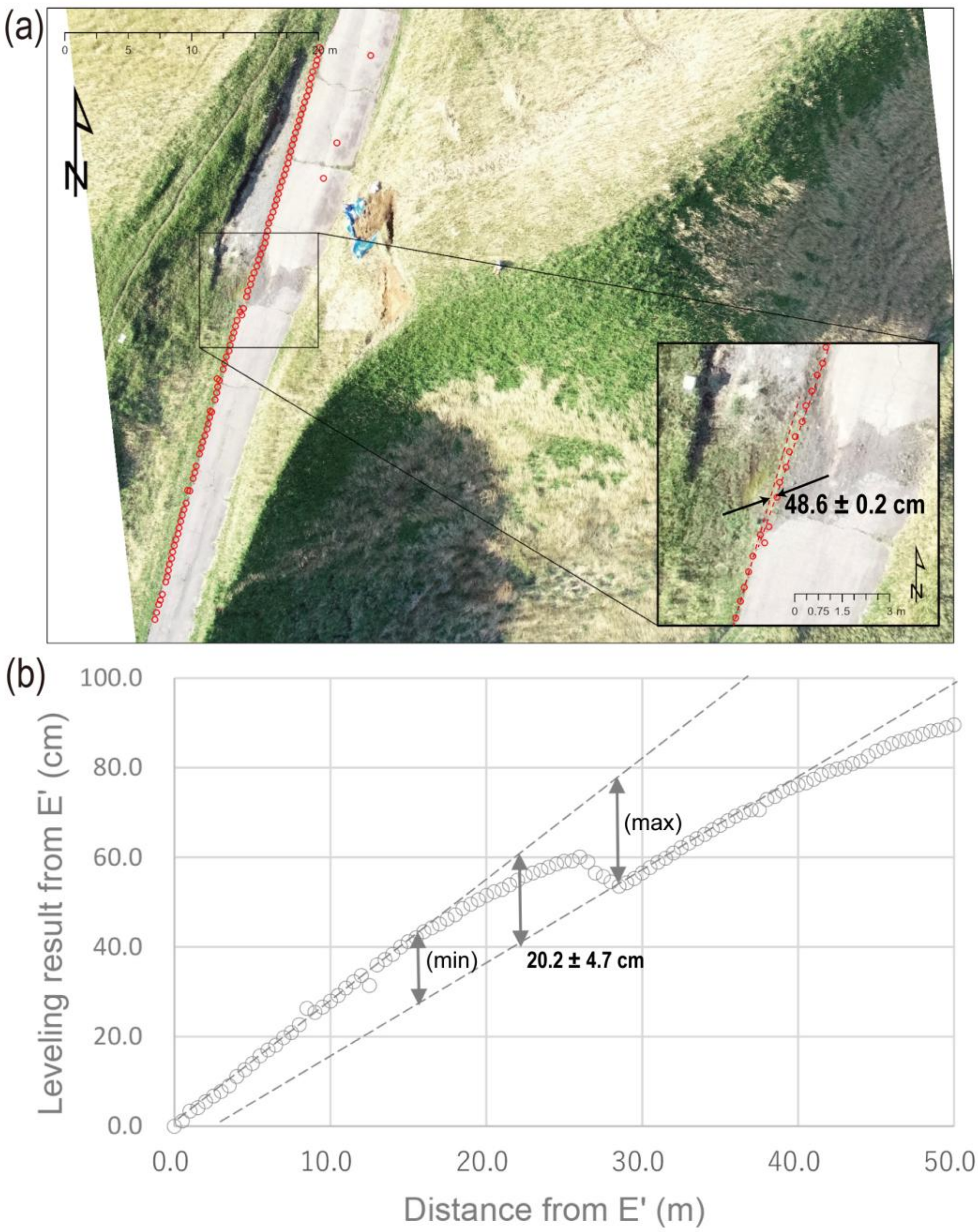

(a)
0 5 10
m
48.6 ± 0.2 cm
0 0.75 1.5 3 m
(b)
Leveling result from E' (cm)
100.0
80.0
60.0
40.0
20.0
0.0
0.0 10.0 20.0 30.0 40.0 50.0
Distance from E' (m)
(max)
(min)
20.2 ± 4.7 cm

Figure 7

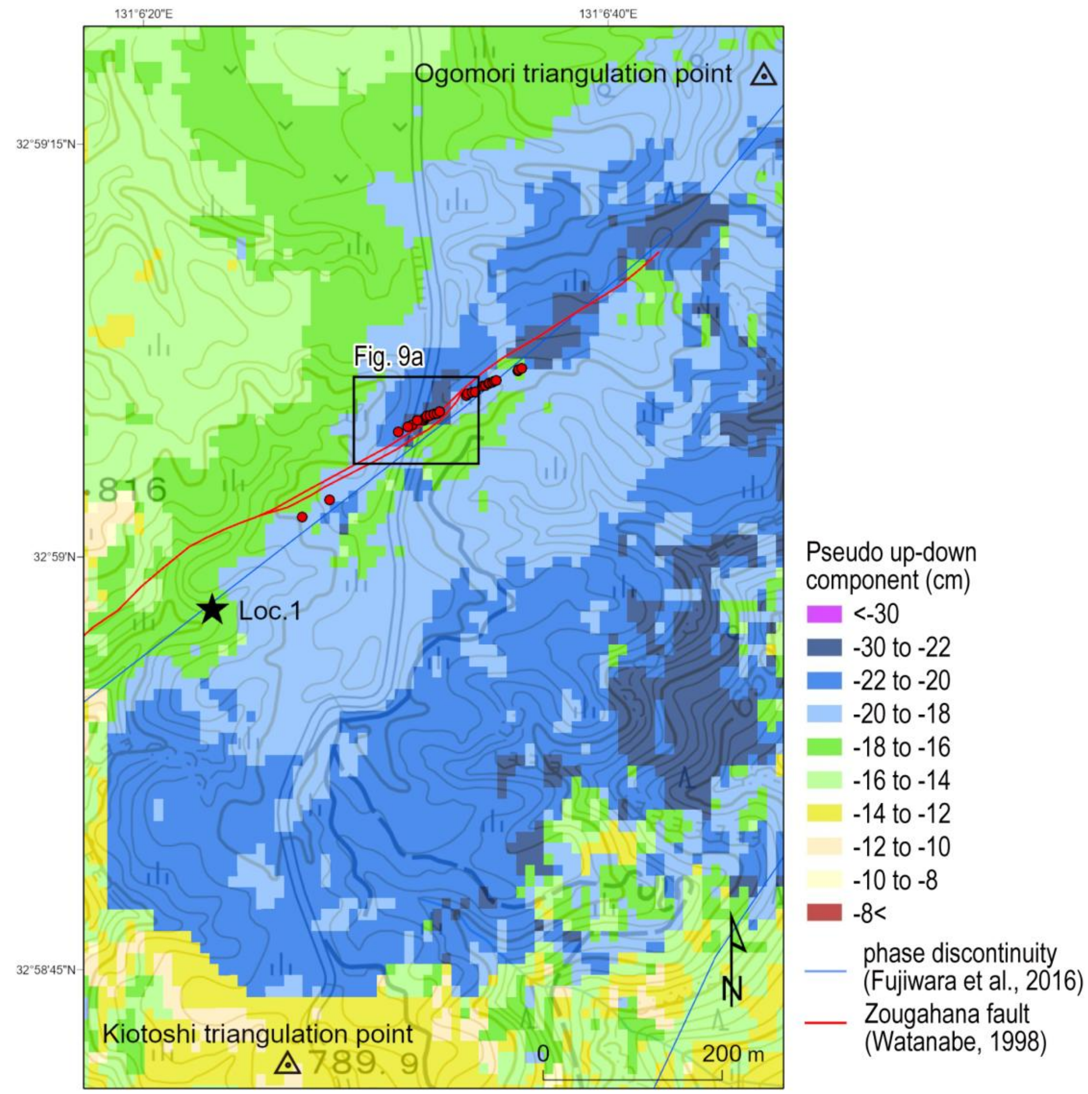
131°6'20"E
131°6'40"E
32°59'15"N
32°59'N
32°58'45"N
Ogomori triangulation point
Fig. 9a
Loc.1
Kiotoshi triangulation point
0
200 m
N
Pseudo up-down component (cm)
<-30
-30 to -22
-22 to -20
-20 to -18
-18 to -16
-16 to -14
-14 to -12
-12 to -10
-10 to -8
-8<
phase discontinuity (Fujiwara et al., 2016)
Zougahana fault (Watanabe, 1998)

Figure 8

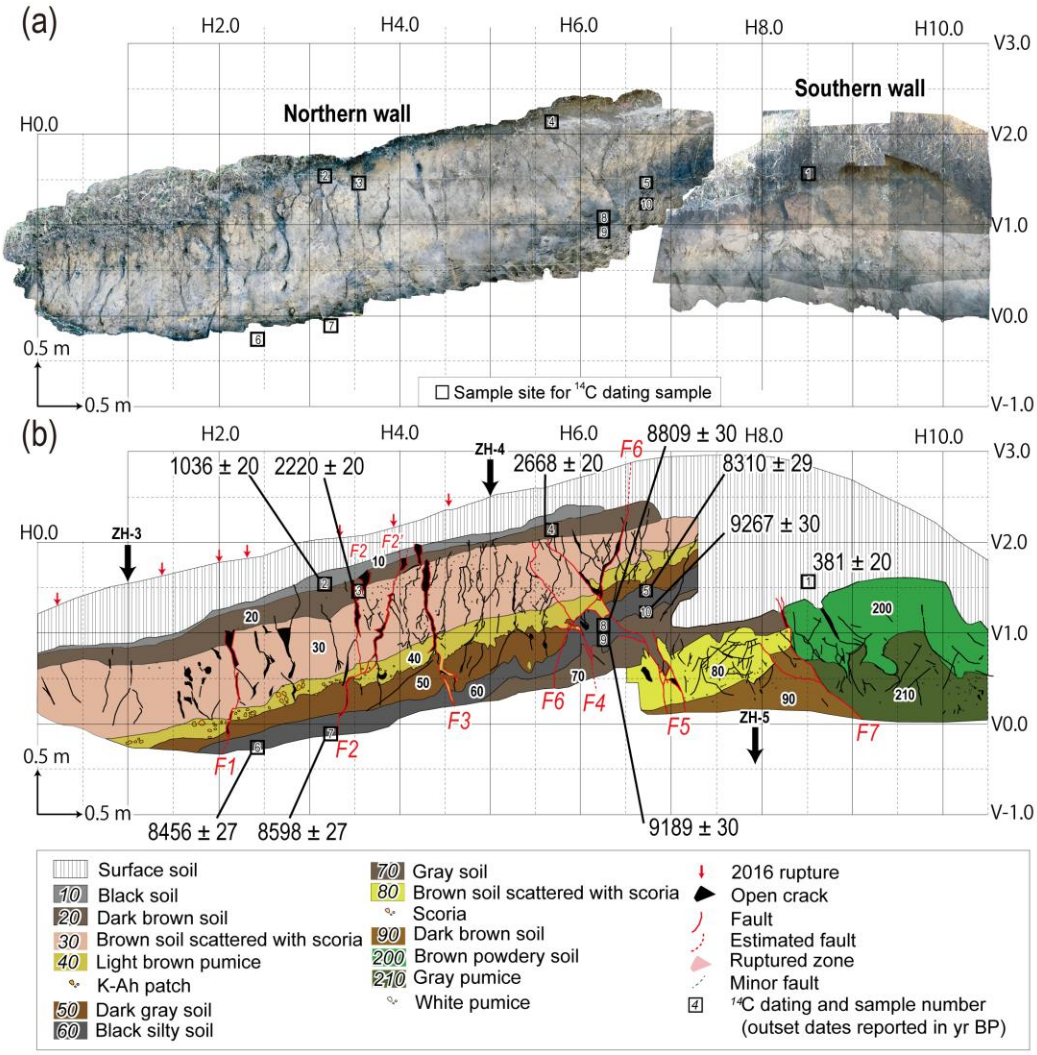

(a)
H0.0
H2.0
H4.0
H6.0
H8.0
H10.0
V3.0
V2.0
V1.0
V0.0
V-1.0
Northern wall
Southern wall
0.5 m
0.5 m
Sample site for 14C dating sample
(b)
ZH-3
ZH-4
ZH-5
1036 ± 20
2220 ± 20
2668 ± 20
8809 ± 30
8310 ± 29
9267 ± 30
381 ± 20
8456 ± 27
8598 ± 27
9189 ± 30
F1
F2
F2'
F3
F4
F5
F6
F7
Surface soil
10 Black soil
20 Dark brown soil
30 Brown soil scattered with scoria
40 Light brown pumice
K-Ah patch
50 Dark gray soil
60 Black silty soil
70 Gray soil
80 Brown soil scattered with scoria
Scoria
90 Dark brown soil
200 Brown powdery soil
210 Gray pumice
White pumice
2016 rupture
Open crack
Fault
Estimated fault
Ruptured zone
Minor fault
14C dating and sample number
(outset dates reported in yr BP)

Figure 9

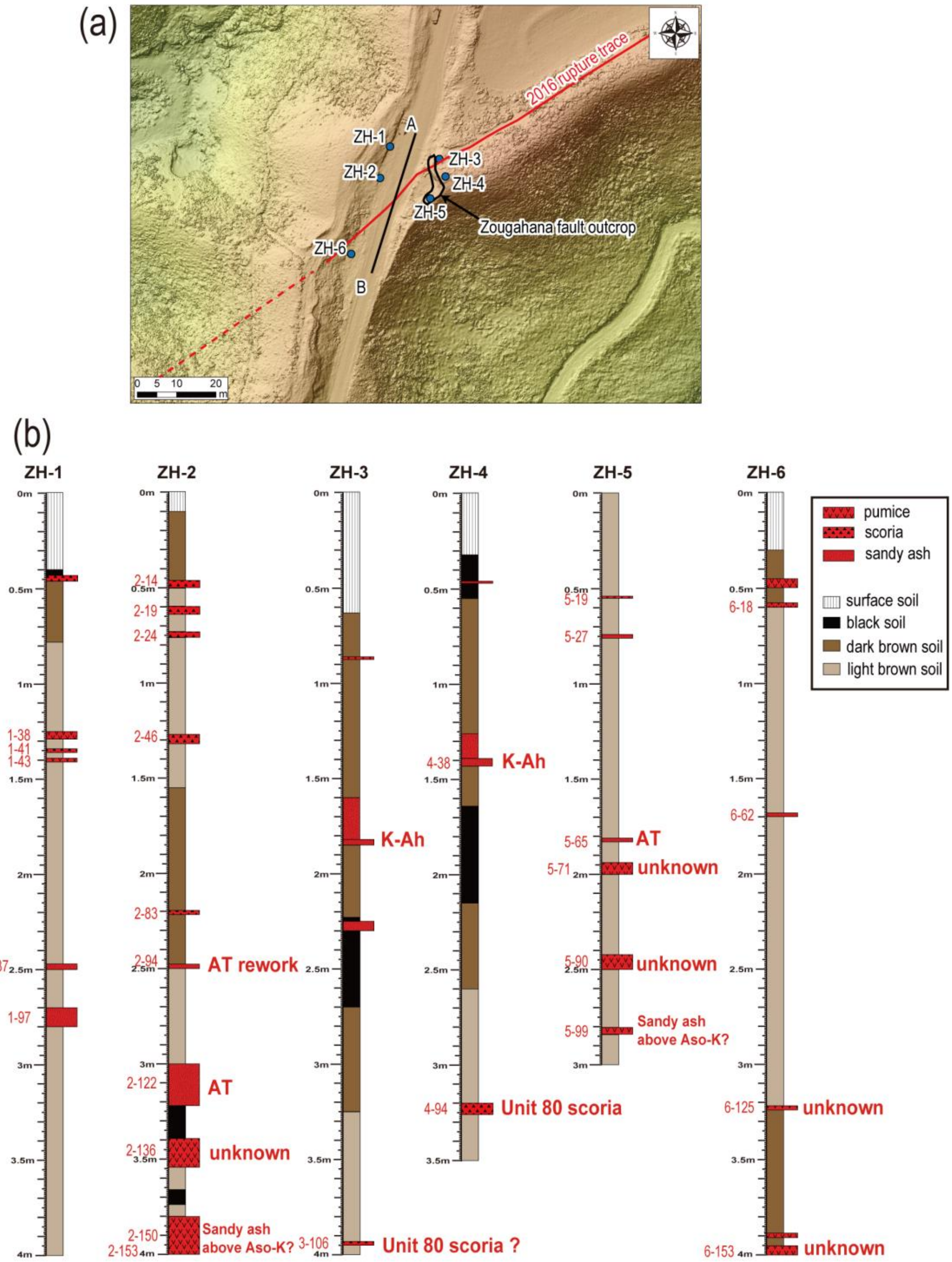
(a)
2016 rupture trace
ZH-1
ZH-2
ZH-3
ZH-4
ZH-5
ZH-6
A
B
Zougahana fault outcrop
0 5 10 20 m
(b)
ZH-1
ZH-2
ZH-3
ZH-4
ZH-5
ZH-6
0m
0.5m
1m
1.5m
2m
2.5m
3m
3.5m
4m
1-38
1-41
1-43
1-87
1-97
2-14
2-19
2-24
2-46
2-83
2-94
AT rework
2-122
AT
2-136
unknown
2-150
2-153
Sandy ash above Aso-K?
K-Ah
3-106
Unit 80 scoria ?
4-38
K-Ah
4-94
Unit 80 scoria
5-19
5-27
5-65
AT
5-71
unknown
5-90
unknown
5-99
Sandy ash above Aso-K?
6-18
6-62
6-125
unknown
6-153
unknown
pumice
scoria
sandy ash
surface soil
black soil
dark brown soil
light brown soil

Figure 10

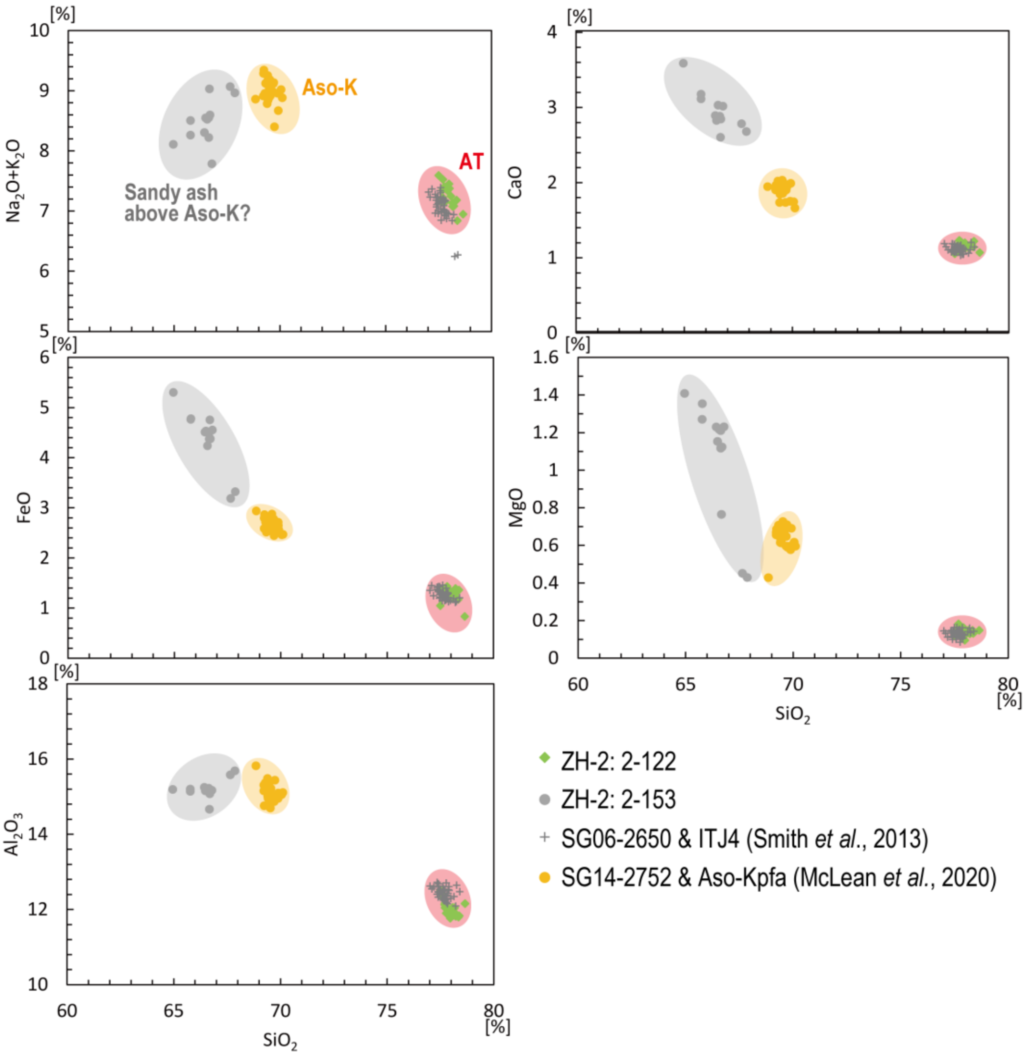

Na2O+K2O
CaO
FeO
MgO
Al2O3
SiO2
[%]
Aso-K
AT
Sandy ash
above Aso-K?
ZH-2: 2-122
ZH-2: 2-153
SG06-2650 & ITJ4 (Smith et al., 2013)
SG14-2752 & Aso-Kpfa (McLean et al., 2020)

Figure 11

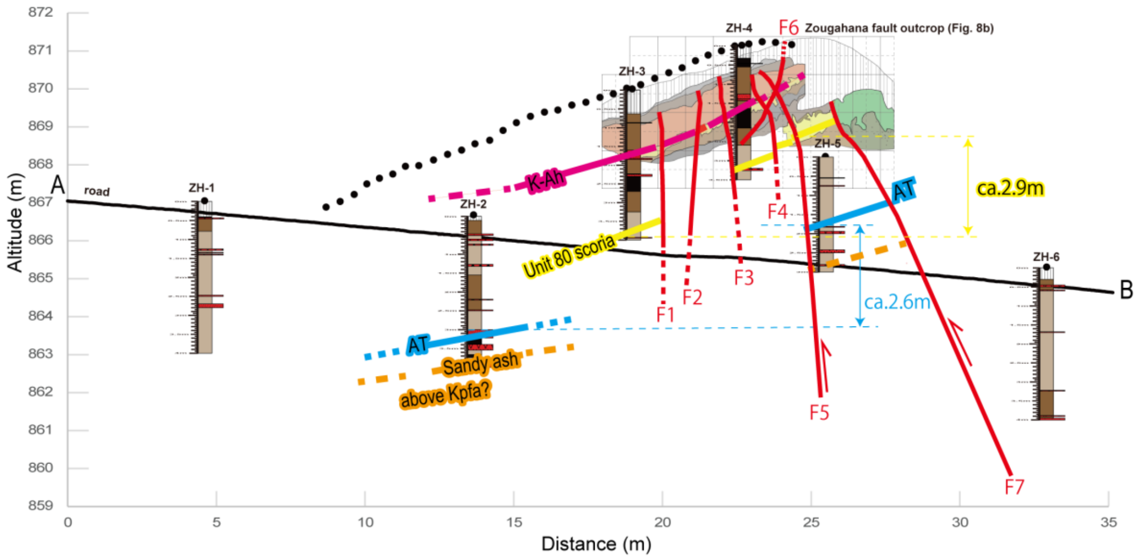

Altitude (m)
Distance (m)
A
road
B
ZH-1
ZH-2
ZH-3
ZH-4
ZH-5
ZH-6
Zougahana fault outcrop (Fig. 8b)
K-Ah
Unit 80 scoria
AT
AT
Sandy ash
above Kpfa?
ca.2.9m
ca.2.6m
F1
F2
F3
F4
F5
F6
F7
872
871
870
869
868
867
866
865
864
863
862
861
860
859
0
5
10
15
20
25
30
35

Figure 12

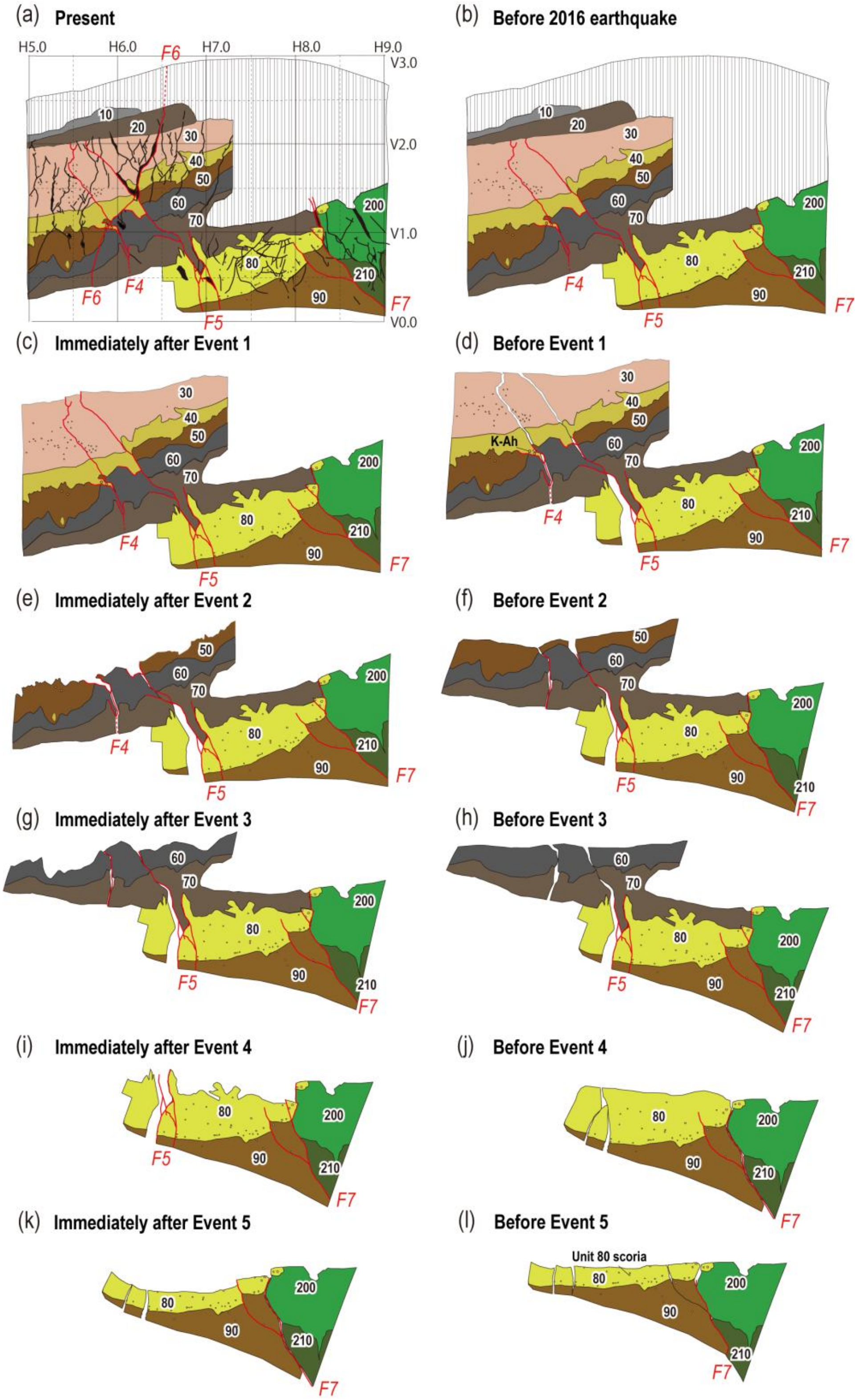

(a) Present
H5.0
H6.0
H7.0
H8.0
H9.0
V3.0
V2.0
V1.0
V0.0
F4
F5
F6
F7
(b) Before 2016 earthquake
(c) Immediately after Event 1
(d) Before Event 1
K-Ah
(e) Immediately after Event 2
(f) Before Event 2
(g) Immediately after Event 3
(h) Before Event 3
(i) Immediately after Event 4
(j) Before Event 4
(k) Immediately after Event 5
(l) Before Event 5
Unit 80 scoria
10
20
30
40
50
60
70
80
90
200
210

Figure 13

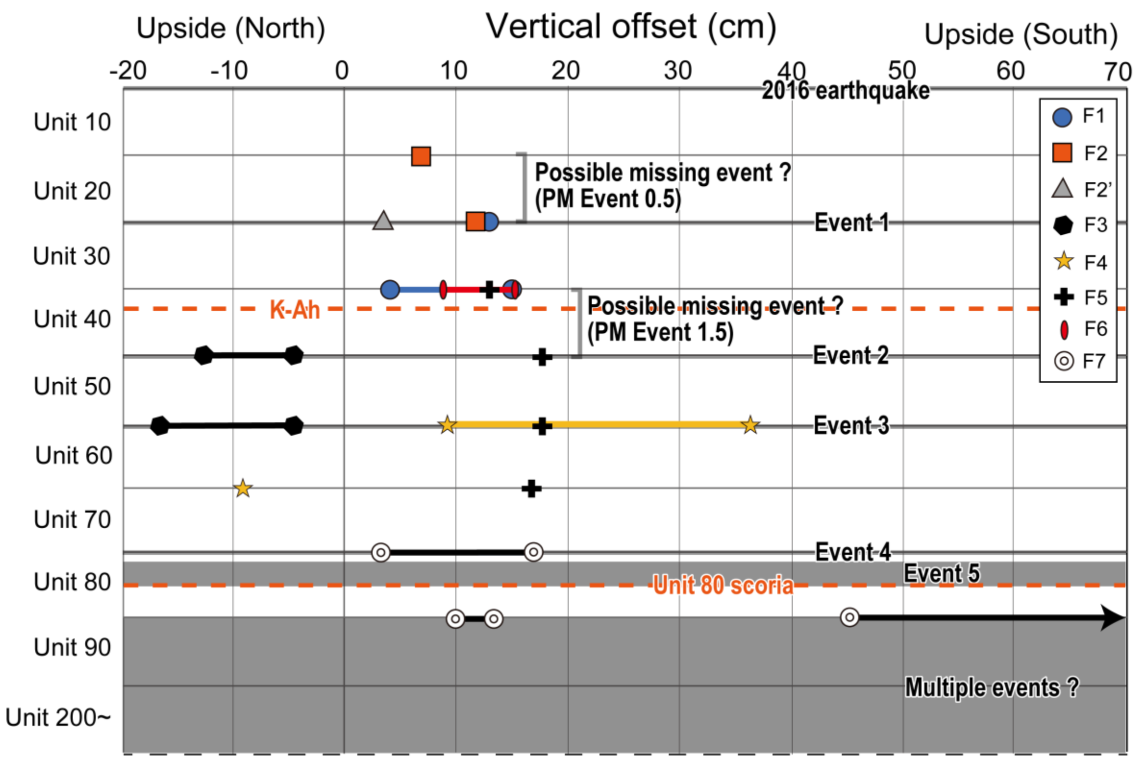

Upside (North)
Vertical offset (cm)
Upside (South)
-20
-10
0
10
20
30
40
50
60
70
2016 earthquake
Unit 10
Unit 20
Unit 30
Unit 40
Unit 50
Unit 60
Unit 70
Unit 80
Unit 90
Unit 200~
Possible missing event ?
(PM Event 0.5)
Event 1
K-Ah
Possible missing event ?
(PM Event 1.5)
Event 2
Event 3
Event 4
Event 5
Unit 80 scoria
Multiple events ?
F1
F2
F2'
F3
F4
F5
F6
F7

Figure 14

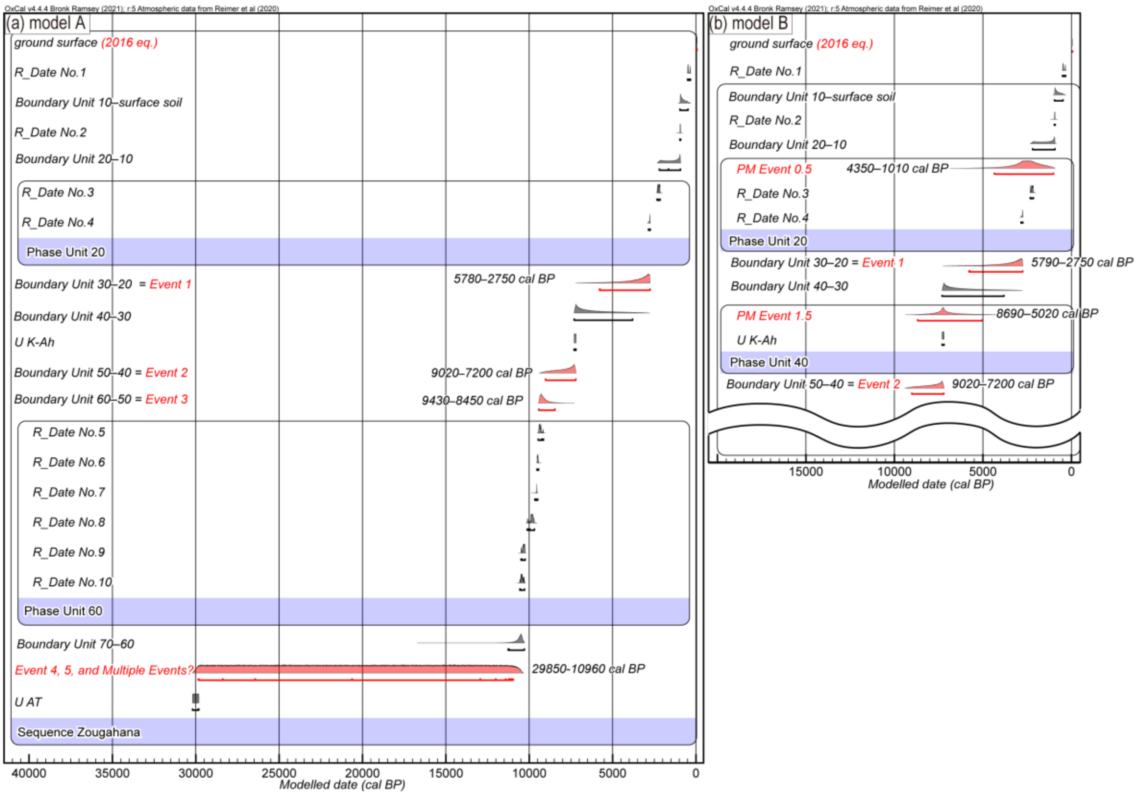

(a) model A
ground surface (2016 eq.)
R_Date No.1
Boundary Unit 10–surface soil
R_Date No.2
Boundary Unit 20–10
R_Date No.3
R_Date No.4
Phase Unit 20
Boundary Unit 30–20 = Event 1
5780–2750 cal BP
Boundary Unit 40–30
U K-Ah
Boundary Unit 50–40 = Event 2
9020–7200 cal BP
Boundary Unit 60–50 = Event 3
9430–8450 cal BP
R_Date No.5
R_Date No.6
R_Date No.7
R_Date No.8
R_Date No.9
R_Date No.10
Phase Unit 60
Boundary Unit 70–60
Event 4, 5, and Multiple Events?
29850-10960 cal BP
U AT
Sequence Zougahana
40000 35000 30000 25000 20000 15000 10000 5000 0
Modelled date (cal BP)
(b) model B
ground surface (2016 eq.)
R_Date No.1
Boundary Unit 10–surface soil
R_Date No.2
Boundary Unit 20–10
PM Event 0.5
4350–1010 cal BP
R_Date No.3
R_Date No.4
Phase Unit 20
Boundary Unit 30–20 = Event 1
5790–2750 cal BP
Boundary Unit 40–30
PM Event 1.5
8690–5020 cal BP
U K-Ah
Phase Unit 40
Boundary Unit 50–40 = Event 2
9020–7200 cal BP
15000 10000 5000 0
Modelled date (cal BP)

Figure 15

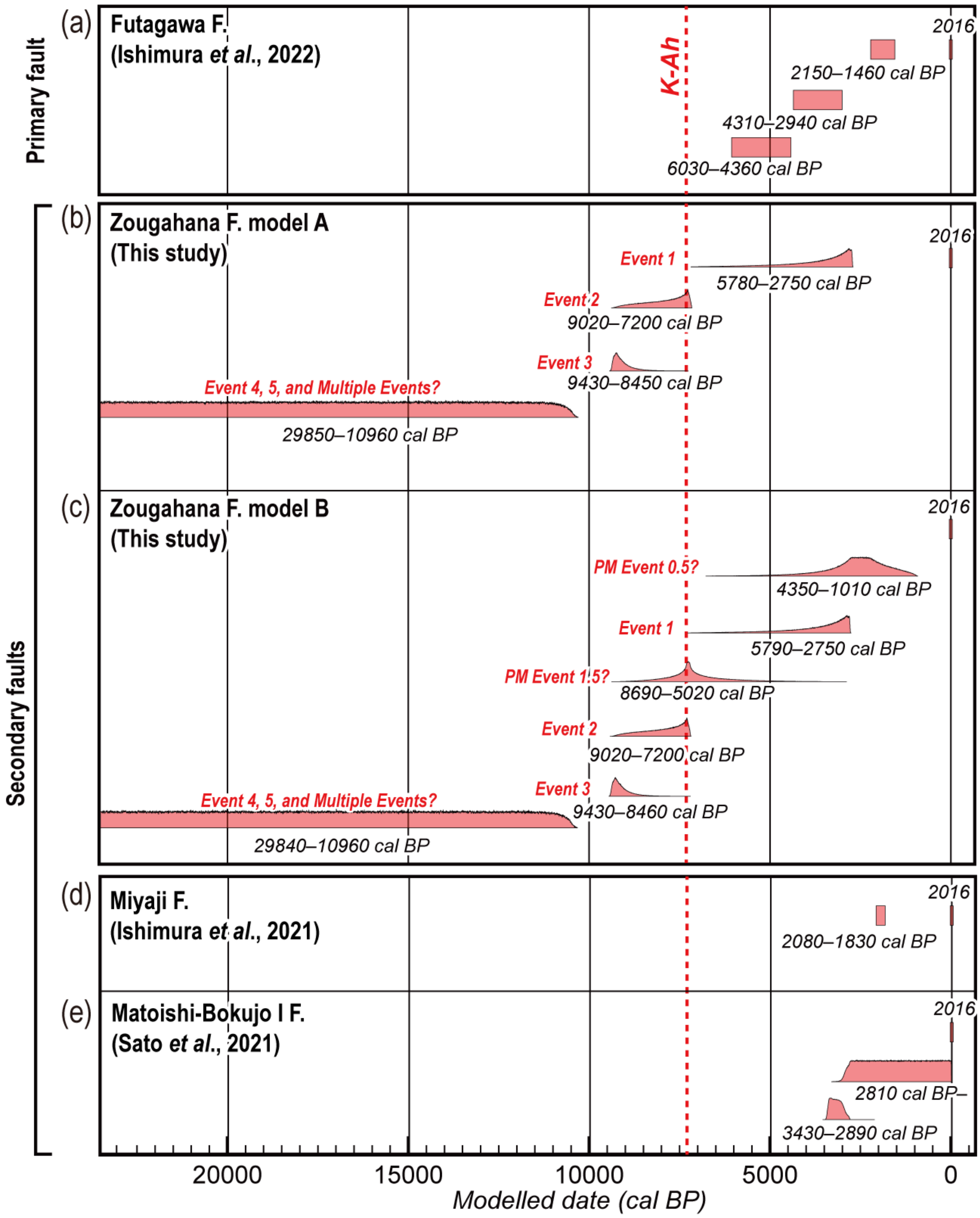
Primary fault
Secondary faults
(a)
Futagawa F.
(Ishimura et al., 2022)
K-Ah
2016
2150–1460 cal BP
4310–2940 cal BP
6030–4360 cal BP
(b)
Zougahana F. model A
(This study)
2016
Event 1
5780–2750 cal BP
Event 2
9020–7200 cal BP
Event 3
9430–8450 cal BP
Event 4, 5, and Multiple Events?
29850–10960 cal BP
(c)
Zougahana F. model B
(This study)
2016
PM Event 0.5?
4350–1010 cal BP
Event 1
5790–2750 cal BP
PM Event 1.5?
8690–5020 cal BP
Event 2
9020–7200 cal BP
Event 3
9430–8460 cal BP
Event 4, 5, and Multiple Events?
29840–10960 cal BP
(d)
Miyaji F.
(Ishimura et al., 2021)
2016
2080–1830 cal BP
(e)
Matoishi-Bokujo I F.
(Sato et al., 2021)
2016
2810 cal BP–
3430–2890 cal BP
20000
15000
10000
5000
0
Modelled date (cal BP)

Figure 16

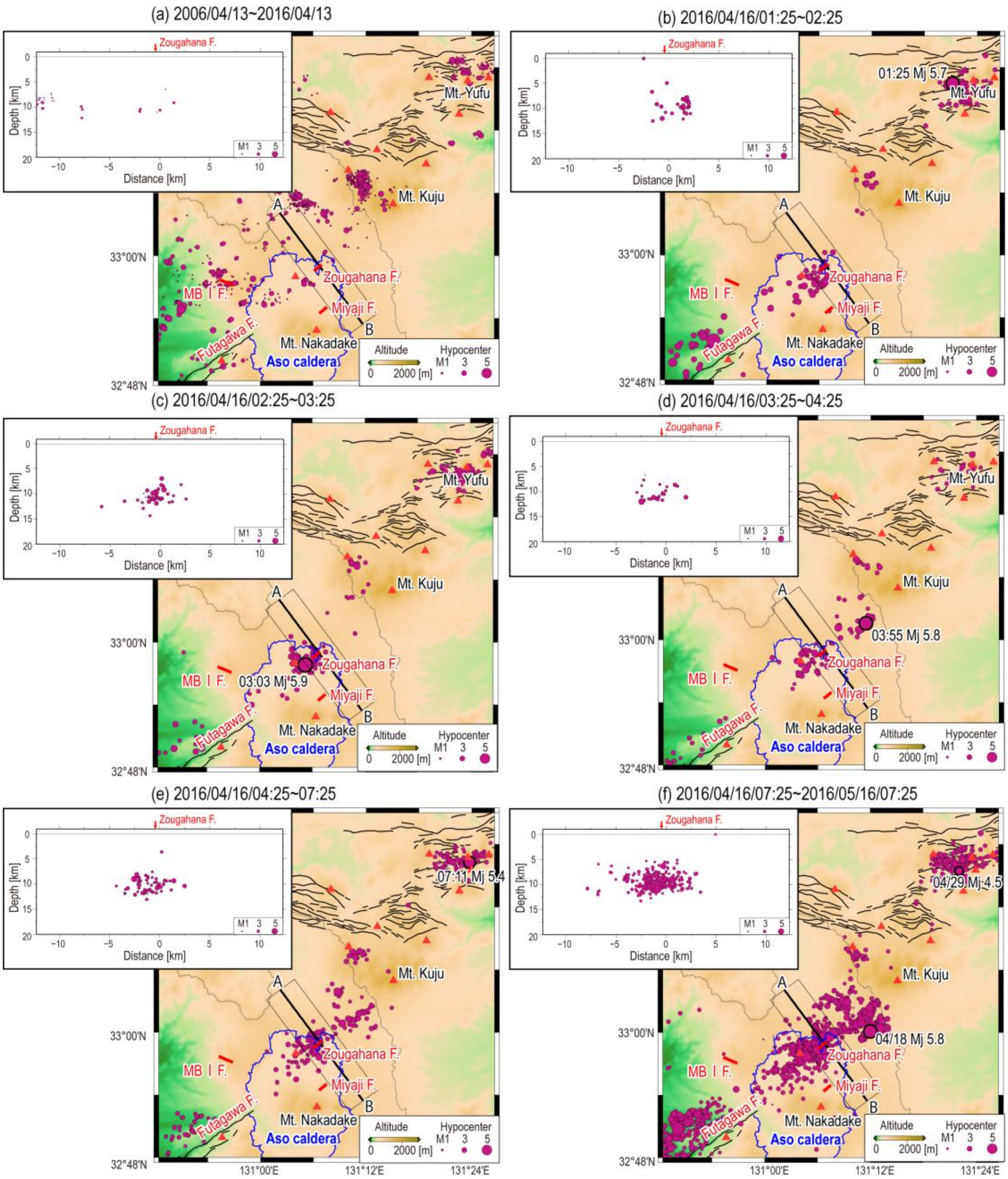

(a) 2006/04/13~2016/04/13
(b) 2016/04/16/01:25~02:25
(c) 2016/04/16/02:25~03:25
(d) 2016/04/16/03:25~04:25
(e) 2016/04/16/04:25~07:25
(f) 2016/04/16/07:25~2016/05/16/07:25
Zougahana F.
Depth [km]
Distance [km]
Mt. Yufu
Mt. Kuju
Zougahana F.
Miyaji F.
MB I F.
Futagawa F.
Mt. Nakadake
Aso caldera
Altitude
0 2000 [m]
Hypocenter
M1 3 5
A
B
01:25 Mj 5.7
03:03 Mj 5.9
03:55 Mj 5.8
07:11 Mj 5.4
04/29 Mj 4.5
04/18 Mj 5.8
33°00'N
32°48'N
131°00'E
131°12'E
131°24'E

1630 Figure 17

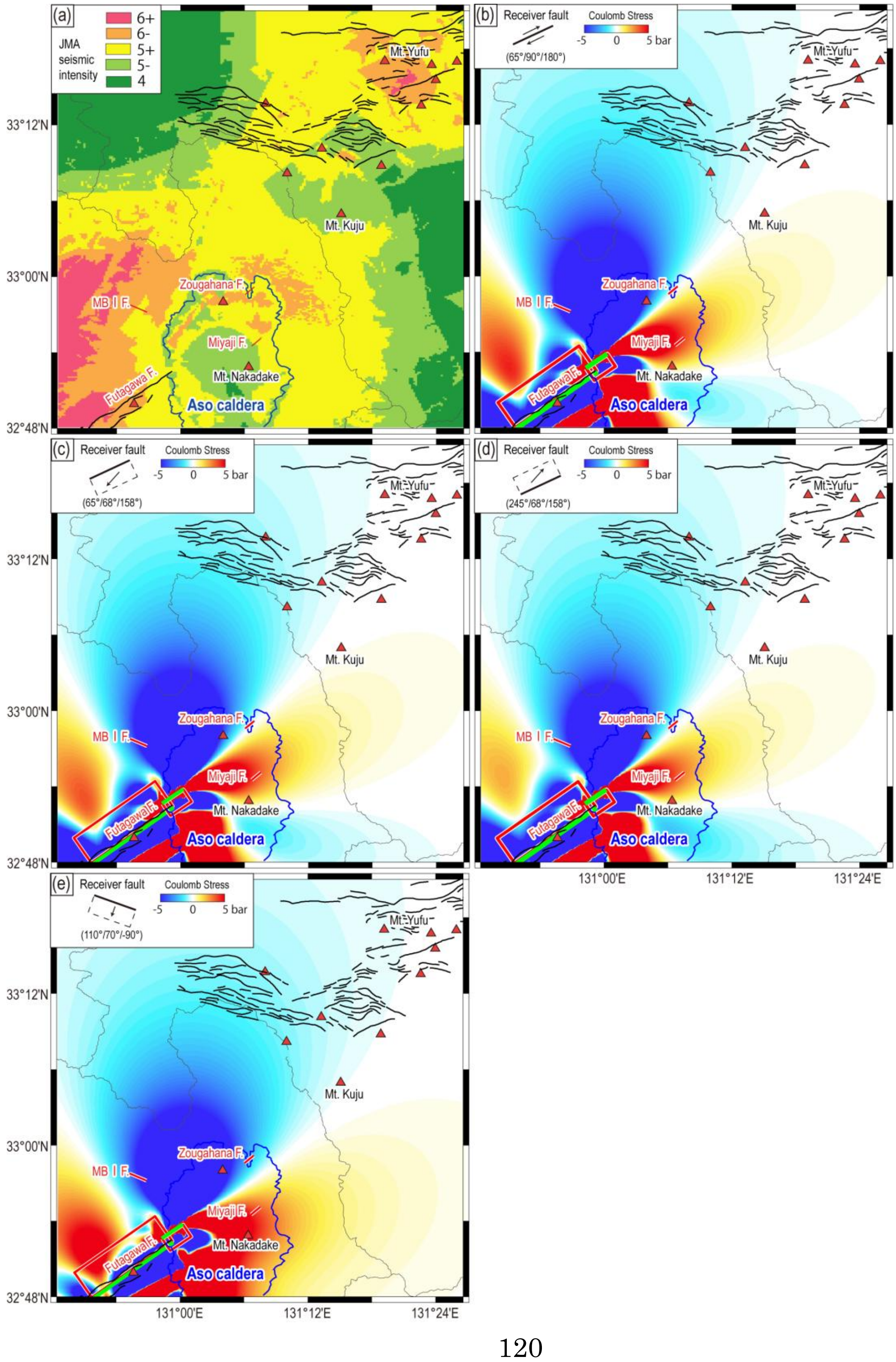

1631

1632 Figure 18

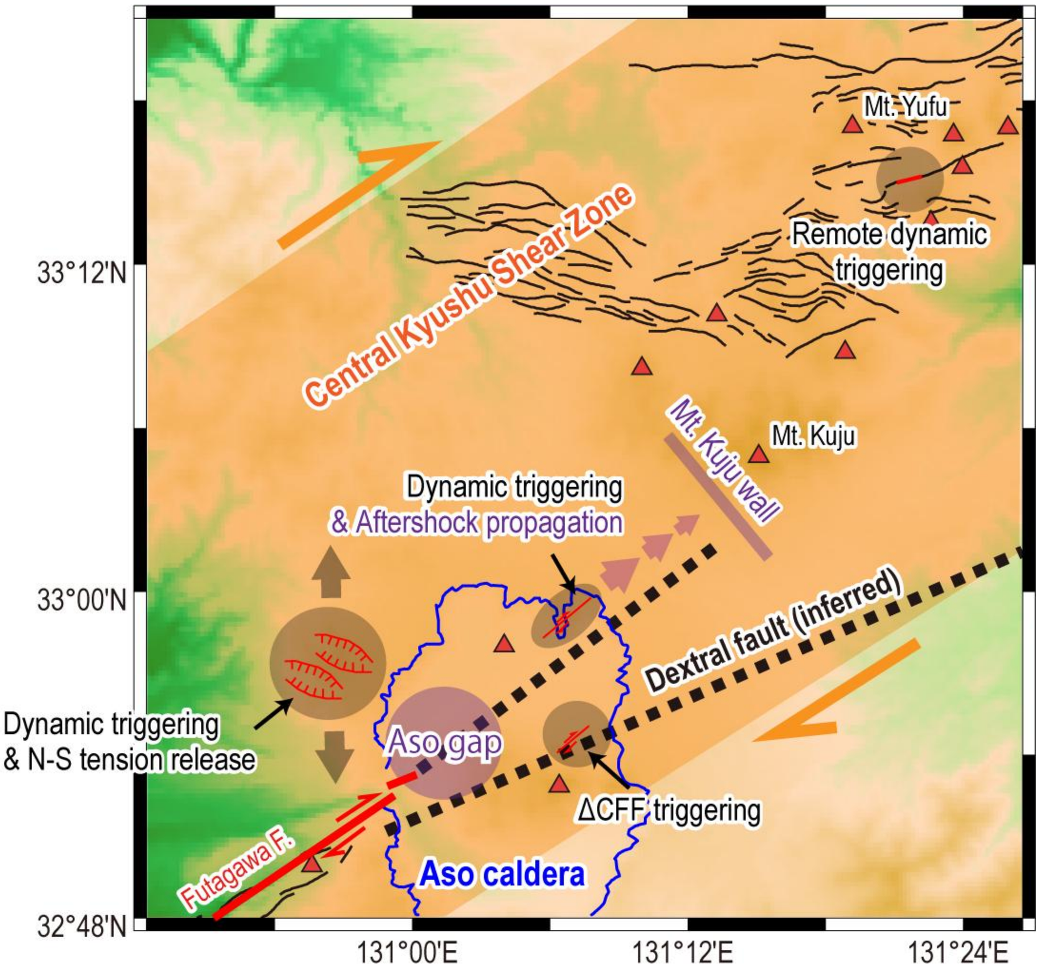

1633